CHAPTER 1

ULTRAFAST AND EFFICIENT CONTROL OF COHERENT ELECTRON DYNAMICS VIA SPODS

Tim Bayer[2], Matthias Wollenhaupt[2], Hendrike Braun[1] and Thomas Baumert[1]

[1]Universität Kassel, Institut für Physik und CINSaT, Heinrich-Plett-Str. 40, 34132 Kassel, Germany

[2]Carl von Ossietzky Universität Oldenburg, Institut für Physik, Carl-von-Ossietzky-Str. 9-11, 26129 Oldenburg, Germany

Abstract. Direct manipulation of charge oscillations in atoms and molecules has emerged as a remarkable perspective in coherent control of photophysical processes. These oscillations have a typical Bohr period of around 1 fs for valence electrons; therefore, control has to be exerted on a shorter timescale. Non-perturbative excitation with precisely shaped intense femtosecond laser pulses is used to induce these charge oscillations as well as to efficiently steer population to different target states. Alignment or anti-alignment of the laser's electric field with respect to the induced dipole-moment decreases or increases the interaction energy, respectively, which eventually gives access to the population of different target states. This classical picture of the physical mechanism is verified by solving the time-dependent Schrödinger equation, where the dressed state representation shows the closest resemblance with the classical one. Selective Population of Dressed States (SPODS) gives a one-to-one correspondence to the important aspects of the classical picture. Tunability of this bidirectional Stark effect up to nearly 300 meV, a selectivity of almost up to 100% and a precision down to the sub-10 attosecond regime

is demonstrated experimentally on atoms and molecules with a theoretical efficiency up to 100%. In molecules vibrational wave packet motion alters the Bohr period in addition. We conclude that SPODS with simple ultrashort optimal pulse shapes is suitable for robust laser control of chemical reactions.

1.1 Introduction

Exploiting coherence properties of laser light together with quantum mechanical matter interferences in order to steer a chemical reaction into a pre-defined target channel is the basis of coherent control [1]. The increasing availability of laser sources operating on the time-scale of molecular dynamics, i.e. the femtosecond regime, and the increasing capabilities of shaping light in terms of amplitude, phase and polarization [2, 3, 4, 5, 6, 7, 8] also on the time-scale of molecular dynamics i.e. the research area of femtochemistry [9, 10] brought the temporal aspect of this field to the fore. Here one seeks to actively exert microscopic control over molecular dynamics at the quantum level on intrinsic time-scales. The goal is to steer any type of light-induced molecular processes from an initial state to a pre-defined target state with both high selectivity and high efficiency. Progress in this fast expanding research field is documented in recent text books, [1, 11, 12] review articles [13, 14, 15, 16, 17, 3, 18, 19, 20, 21, 22, 23, 24, 25, 26, 27, 28] and special issues [29, 30, 31, 32, 33]. Optimized light fields can be found for example by employing adaptive feedback learning loops, in cases where knowledge on the photophysical system is limited (black box approach), [34, 35, 36, 37, 38, 39, 40], or by fine tuning the parameters of physically motivated pulse shapes [41, 42, 43, 44, 45], where experimentally determined quantum control landscapes [46, 47] can help identifying the underlying physical mechanisms especially in the strong-field regime.
In contrast to weak-field (perturbative) quantum control schemes where the population of the initial state is approximately constant during the interaction with the external light field, the strong-field (non-perturbative) regime is characterized by efficient population transfer. Adiabatic strong-field techniques such as Rapid Adiabatic Passage (RAP) or Stimulated Raman Adiabatic Passage [48, 49] are employed for instance with laser pulses in the picosecond [50, 51, 52, 3] to nanosecond domain allowing for population transfer with unit efficiency in quantum systems. As compared to direct control of population via resonantly excited Rabi oscillations, these adiabatic techniques are attractive because of their robustness with respect to experimental imperfections. Only recently these techniques were transferred to the femtosecond regime. For example selectivity based on (dynamic Stark shifted) RAP combined with high efficiency was demonstrated in an atomic ladder system with the help of chirped laser pulses [53] and Piecewise Adiabatic Passage (PAP) was demonstrated in an atomic two level system with chirped pulse sequences [54]. Furthermore it was shown that effects of dynamic Stark shift reducing the excitation efficiency, can be compensated with temporally structured

pulses [55].
The modification of the electronic potentials due to the interaction with the electric field of the laser pulse has another important aspect pertaining to molecules, as the nuclear motion can be significantly altered in light induced potentials. Experimental examples for modifying the course of reactions of neutral molecules after an initial excitation via altering the potential surfaces can be found in [56, 57] where the amount of initial excitation on the molecular potential can be set via Rabi type oscillations [58]. Non-resonant interaction with an excited vibrational wavepacket can in addition change the population of the vibrational states [59]. Note, that this non-resonant Stark control acts on the time-scale of the intensity envelope of an ultrashort laser pulse [60].
The emerging field of attosecond science [61, 62, 63, 64] provided the possibility to directly observe ultrafast electron dynamics. Because of the high photon energies, however, the excitation of outer shell electrons by attosecond laser fields suffers from low cross-sections and is likely to cause direct ionization, which hampers the implementation of valence bond chemistry control schemes. On the other hand, electronic transitions of outer shell electrons driven by pico- to femtosecond laser pulses in the UV-VIS-IR spectral regime benefit from large transition moments. This is a prerequisite for efficient population transfer and thus to achieve efficient product yields in reaction control. In addition, as mentioned above, non-perturbative strong laser fields alter the potential energy surface via dynamic Stark shifts, exploring new routes to different target states inaccessible in the weak-field regime.
Making use of the resonant AC Stark effect is especially attractive to that end, as this effect acts on the time-scale of the electron dynamics (1 fs for valence electrons), and in particular enables Stark shifting of molecular states to higher as well as lower energies i.e. offers bidirectionality [65, 66, 67, 68, 69]. In a classical picture charge oscillations are induced via resonant excitation of the corresponding quantum system, and it is the alignment or anti alignment of the laser's electric field with respect to the induced dipole-moment that decreases or increases the interaction energy, respectively, which eventually provides access to the population of different target states. It will be shown below, that this classical picture of the physical mechanism is verified by solving the time-dependent Schrödinger equation, where the dressed state representation and the selective Population of Dressed States (SPODS) gives an almost one-to-one correspondence to the classical picture.
Switching electronic population to different final states with high efficiency via SPODS is a fundamental resonant strong-field effect as the only requirement is the use of intense ultrashort laser pulses exhibiting temporally varying optical phases, such as phase jumps [67, 68, 70, 71] or chirps [72, 44]. Only recently these concepts were transferred to molecules where the coupled electron nuclear dynamics have to be considered in addition [73, 74].

In Fig. 1.1 the general strong-field control scheme for ultrafast efficient switching of electronic excitation via SPODS is depicted. The target states $|f_n\rangle$ are populated via a two photon non-perturbative interaction out of the

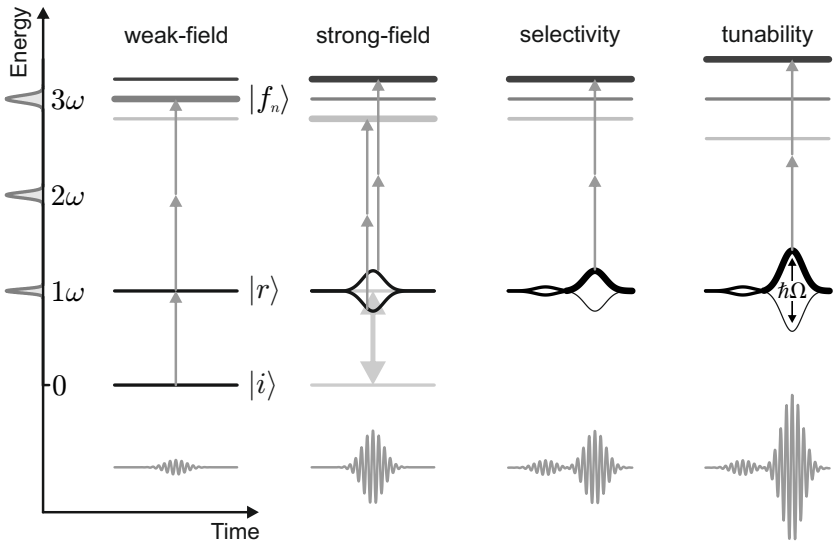

Figure 1.1 General strong-field control scheme for ultrafast efficient switching of electronic excitation. A shaped femtosecond laser pulse steers the quantum system from an initial state $|i\rangle$ via the intermediate resonant state $|r\rangle$ to a final state $|f_n\rangle$ out of a manifold of target states. Intense laser fields alter the energy landscape of the system by virtue of the resonant AC Stark effect. As a result new target states, which lie outside the laser spectral bandwidth, become energetically accessible. Selective Population of Dressed States (SPODS) in the resonant sub-system enables the selective and efficient excitation of a single target state. Manipulation of the dressed state energies by adjustment of the Rabi frequency, i.e. the laser field amplitude, provides tunability among the target states.

strongly coupled intermediate resonant state $|r\rangle$ where control is exerted on. This scheme illustrates SPODS in the most transparent way: in general, strong laser fields give rise to an energy splitting of the resonant state into two (dressed) states in the order of $\hbar\Omega$, where Ω describes the Rabi-frequency. The decisive step in switching among different final electronic states is realized by manipulation of dressed state energies and dressed state populations. By suitable phase shaping of the driving laser field, it is possible to populate only one of these two dressed states, i.e., to realize SPODS. Effectively, population of a single dressed state corresponds to a controlled energy shift of the resonant state into a desired direction as illustrated in Fig. 1.1. With the help of this scheme, we demonstrate tunability of this bidirectional Stark effect up to nearly 300 meV, a selectivity of almost up to 100% and a precision down to the sub-10 attosecond regime experimentally on atoms (see Secs. 1.5.1 to 1.5.3).

In Fig. 1.2 the SPODS concept for control of photochemical reactions by the steering of electron dynamics is illustrated taking a fully non-perturbative approach including molecular dynamics into account. Experimental results

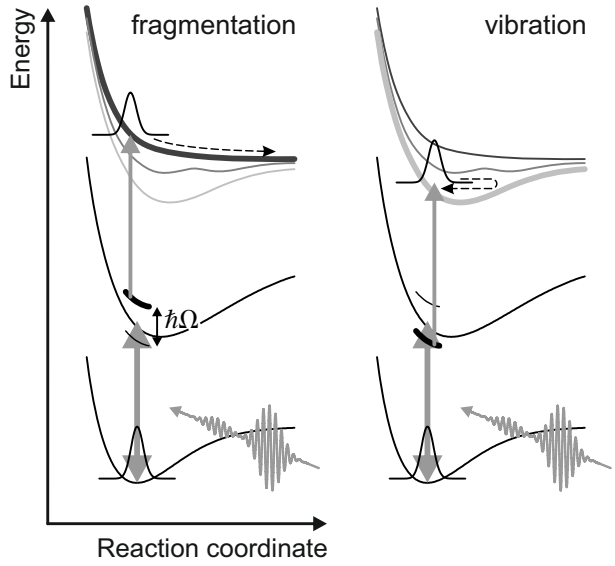

Figure 1.2 Steering of photochemical reactions by coherent control of ultrafast electron dynamics in molecules by shaped femtosecond laser pulses. Ultrafast excitation of electronic target states in molecules launches distinct nuclear dynamics which eventually lead to specific outcomes of the photochemical reaction. The ability to switch efficiently between different electronic target channels, optimally achieved by turning only a single control knob on the control field, provides an enhanced flexibility in the triggering of photochemical events, such as fragmentation, excited state vibration, isomerization, etc..

obtained on charge oscillation controlled molecular excitation are presented in Sec. 1.6.

In the following, we start in Sec. 1.2 by introducing the general concepts of ultrafast pulse shaping, and discuss two different prototype pulse shapes used later in the SPODS experiments, where the time-varying optical phase required for SPODS is implemented either by discrete temporal phase jumps (Sec. 1.2.1) or continuous frequency chirps (Sec. 1.2.2). In Sec. 1.3 we discuss phase control i.e. SPODS on theoretical model systems. We start with a classical model in Sec. 1.3.1 and turn to the quantum mechanical description of a resonantly coupled two-state system in Sec. 1.3.2, showing the similarities when the dressed state representation is employed. SPODS based on phase jumps, realizing Photon Locking (PL), and based on chirps, realizing RAP, is discussed within that context. In Sec. 1.3.3 a five-state system is studied and PL as well as RAP scenarios are discussed in view of the selective excitation of different final states, achieving population transfer efficiencies of 100%. After a description of our experimental setup in Sec. 1.4 we demonstrate the experimental implementation of the general SPODS scheme presented in Fig. 1.1 on

K atoms in Sec. 1.5 and the ultrafast efficient switching of concerted electron-nuclear dynamics in K_2 molecules in Sec. 1.6. Some concluding remarks are given in Sec. 1.7.

1.2 Ultrafast Pulse Shaping

As mentioned in the introduction the ability to shape femtosecond laser pulses with unprecedented precision is the key to efficient control of photophysical and photochemical processes at the quantum level. In this section we present the fundamentals of femtosecond pulse shaping and introduce specific pulse shapes that are used in the experiments and simulations presented in the following sections. We start with the electric field of a Bandwidth-Limited (BWL) femtosecond laser pulse written in terms of its positive frequency analytic signal

$$E^+(t) = \mathcal{E}(t)e^{i\omega_0 t}, \tag{1.1}$$

The pulse has a real-valued envelope $\mathcal{E}(t)$ and oscillates with the carrier frequency ω_0. Because ultrafast laser pulses are too short to be shaped directly in the time domain the pulse is manipulated in the frequency domain. To this end a linear spectral transfer function $\tilde{\mathcal{M}}(\omega)$ is applied to the pulse spectrum $\tilde{\mathcal{E}}(\omega)$, with

$$\tilde{\mathcal{E}}(\omega) = \int_{-\infty}^{\infty} \mathcal{E}(t)e^{-i\omega t}dt \tag{1.2}$$

being the Fourier transform of the temporal envelope $\mathcal{E}(t)$. The practical implementation of this procedure will be described in Sec. 1.4. Multiplication of $\tilde{\mathcal{E}}(\omega)$ by $\tilde{\mathcal{M}}(\omega)$ yields the modulated pulse spectrum

$$\tilde{\mathcal{E}}^+_{\mathrm{mod}}(\omega) = \tilde{\mathcal{M}}(\omega) \cdot \tilde{\mathcal{E}}(\omega). \tag{1.3}$$

In the experiments we use phase-only modulation realized by transfer functions of the form

$$\tilde{\mathcal{M}}(\omega) = e^{-i\varphi(\omega)}. \tag{1.4}$$

Here we introduced the spectral phase-modulation function $\varphi(\omega)$ which is used to parameterize the laser pulse shape. Since $|\tilde{\mathcal{M}}(\omega)| \equiv 1$ in this case, the modulus of the pulse spectrum – and hence its energy content – remains unaltered by the spectral modulation. The modulated pulse envelope in the time domain is obtained by inverse Fourier transformation

$$\mathcal{E}^+_{\mathrm{mod}}(t) = \frac{1}{2\pi}\int_{-\infty}^{\infty} \tilde{\mathcal{E}}^+_{\mathrm{mod}}(\omega)e^{i\omega t}d\omega = \mathcal{M}(t) * \mathcal{E}(t), \tag{1.5}$$

where $\mathcal{M}(t)$ is the inverse Fourier transform of $\tilde{\mathcal{M}}(\omega)$ and '$*$' denotes the convolution. In general the modulated envelope is complex-valued and may be written in polar representation as

$$\mathcal{E}^{+}_{\mathrm{mod}}(t) = \left|\mathcal{E}^{+}_{\mathrm{mod}}(t)\right| e^{i\zeta(t)}. \tag{1.6}$$

While the modulus $\left|\mathcal{E}^{+}_{\mathrm{mod}}(t)\right|$ describes the temporal amplitude of the shaped pulse, the temporal phase $\zeta(t)$ contains all information about its frequency sweep. Introducing the temporal detuning $\Delta(t) = \dot{\zeta}(t)$ the generally time-dependent instantaneous frequency of the pulse reads

$$\omega_{\mathrm{inst}}(t) = \omega_0 + \Delta(t). \tag{1.7}$$

The real-valued electric field of the shaped laser pulse is given by the real part of the modulated analytic signal:

$$E_{\mathrm{mod}}(t) = 2\Re\left[\mathcal{E}^{+}_{\mathrm{mod}}(t)\, e^{i\omega_0 t}\right] = 2\left|\mathcal{E}^{+}_{\mathrm{mod}}(t)\right| \cdot \cos[\omega_0 t + \zeta(t)]. \tag{1.8}$$

In the following we describe two prominent types of spectral phase-modulation, each of which plays an important role in coherent control. Both types, namely sinusoidal (Sec. 1.2.1) and quadratic (Sec. 1.2.2) spectral phase-modulation, are relevant for the experiments and simulations presented in this contribution. We provide analytic expressions for the modulated laser fields in the time domain and briefly discuss the main characteristics of both classes of pulse shapes.

1.2.1 Sinusoidal Spectral Phase-Modulation

Periodic spectral phase-modulation functions have been used in numerous experiments and theoretical studies on coherent control of atoms [75, 76, 77, 78, 79] and molecules [80, 42, 81, 82, 24, 25, 68, 83, 84, 85, 73]. Applying a sinusoidal phase-modulation function of the form

$$\varphi(\omega) = A \cdot \sin(\omega T + \phi) \tag{1.9}$$

to the input pulse spectrum generates the modulated temporal field

$$\mathcal{E}^{+}_{\mathrm{mod}}(t) = \sum_{n=-\infty}^{\infty} J_n(A)\, \mathcal{E}(t - nT)\, e^{-in\phi}, \tag{1.10}$$

where J_n is the Bessel function of the first kind and order n. Eq. (1.10) shows that sinusoidal phase-modulation in the frequency domain produces a sequence of sub-pulses in the time domain with a temporal separation determined by the parameter T and well defined relative temporal phases controlled by the absolute phase ϕ of the sine function. Examples of shaped laser pulses from sinusoidal spectral phase-modulation are shown in Fig. 1.3. Provided

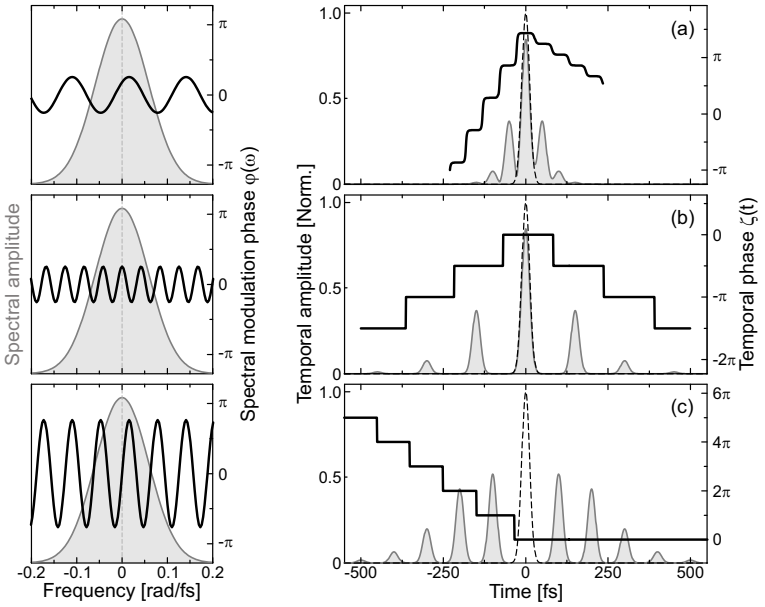

Figure 1.3 Shaped femtosecond laser pulses from sinusoidal spectral phase-modulation of an 800 nm, 20 fs FWHM input pulse. The left column shows the modulated pulses in the frequency domain, decomposed into spectral amplitude $|\tilde{\mathcal{E}}^{+}_{\mathrm{mod}}(\omega)|$ (grey line and background) and modulation phase $\varphi(\omega)$ (black bold line). The resulting temporal fields are shown in the right column decomposed into temporal amplitude $|\mathcal{E}^{+}_{\mathrm{mod}}(t)|$ and phase $\zeta(t)$. As a reference the BWL input pulse is always shown as a dashed line in addition. The spectral modulation paramters are: (a) $A = 0.8$, $T = 50$ fs, $\phi = \pi/4$, (b) $A = 0.8$, $T = 150$ fs, $\phi = \pi/2$ and (c) $A = 2.4$, $T = 100$ fs, $\phi = 0$.

the individual sub-pulses are temporally separated, i.e. $T \gg \Delta t$ if Δt denotes the Full Width at Half Maximum (FWHM) of the intensity of the input pulse, the envelope of each sub-pulse is a scaled and shifted replica of the BWL pulse envelope (see Fig.1.3(b) and (c)). The amplitudes of the sub-pulses are controlled by the modulation parameter A via the Bessel function $J_n(A)$. If the temporal separation of the pulses is smaller than the pulse duration, i.e. $T \lesssim \Delta t$, the sub-pulses with different phases overlap giving rise to a complicated temporal profile and variations of the instantaneous frequency (see Fig.1.3(a)). A more detailed description of the effect of sinusoidal phase-modulation can be found in [79] and [46]. Experiments and theoretical studies on coherent control of ultrafast electron dynamics by intense sinusoidally modulated fields will be discussed in Secs. 1.3.2.2, 1.3.3.1 and 1.6.

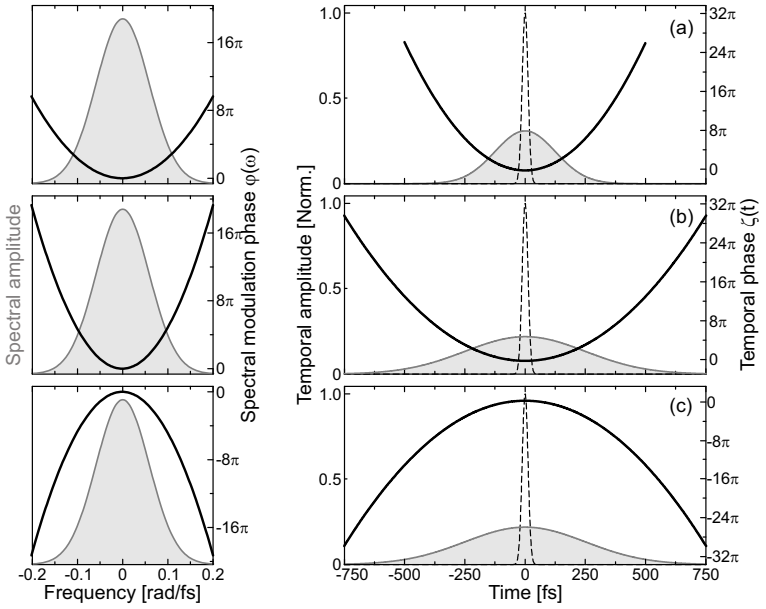

Figure 1.4 Shaped femtosecond laser pulses from quadratic spectral phase-modulation of an 800 nm, 20 fs FWHM input pulse, shown as dashed line in the right column. The assignment of quantities is the same as in Fig. 1.3. The three cases correspond to different chirp parameters of (a) $\phi_2 = 1500$ fs^2, (b) $\phi_2 = 3000$ fs^2 and (c) $\phi_2 = -3000$ fs^2

1.2.2 Quadratic Spectral Phase-Modulation

Quadratic phase-modulation using the spectral phase-modulation function

$$\varphi(\omega) = \frac{\phi_2}{2} \cdot \omega^2 \tag{1.11}$$

plays a major role in coherent control (see for example [86, 87, 88, 89, 72, 53]). Assuming a Gaussian-shaped input pulse with a peak amplitude of $\mathcal{E}_0$ and a FWHM of the intensity Δt

$$\mathcal{E}_G(t) = \mathcal{E}_0\, e^{-\ln(4)\left(\frac{t}{\Delta t}\right)^2} \tag{1.12}$$

the modulated pulse remains Gaussian-shaped and reads

$$\mathcal{E}^+_{\mathrm{mod}}(t) = \mathcal{E}_0\, \gamma^{-\frac{1}{4}}\, e^{-\frac{t^2}{4\beta\gamma}}\, e^{i(\alpha t^2 - \varepsilon)}, \tag{1.13}$$

where we used the abbreviations

$$\alpha = \frac{\phi_2}{8\beta^2\gamma}, \quad \beta = \frac{\Delta t^2}{8\ln(2)}, \quad \gamma = 1 + \frac{\phi_2^2}{4\beta^2} \quad \text{and} \quad \varepsilon = \frac{1}{2}\arctan\left(\frac{\phi_2}{2\beta}\right). \tag{1.14}$$

As a consequence of the spectral modulation, the temporal width of the laser pulse is modified and a linear frequency sweep (chirp) is introduced. The modulated pulse duration is

$$\Delta t_{\mathrm{mod}} = \Delta t \cdot \sqrt{1 + \left(\ln(16)\frac{\phi_2}{\Delta t^2}\right)^2} \tag{1.15}$$

which describes an additional lengthening due to the chirp. The frequency sweep is characterized by a linear change of the instantaneous detuning

$$\Delta(t) = 2\alpha t. \tag{1.16}$$

The parameter

$$\alpha = \left[2\phi_2 + \frac{\Delta t^4}{8\ln^2(2)\phi_2}\right]^{-1} \tag{1.17}$$

describes the chirp rate. Eq. (1.17) shows that the chirp rate is a non-monotonic function of the chirp parameter ϕ_2. A positive value of ϕ_2 leads to an "up-chirp" characterized by an increase of the instantaneous frequency. Examples of up-chirped pulses for two different chirp parameters ϕ_2 are displayed in Fig. 1.4(a) and (b). With increasing chirp parameter ϕ_2, the pulse duration increases according to Eq. (1.15) accompanied by a reduction in intensity. A negative ϕ_2 implies a decrease of $\Delta(t)$, known as "down-chirp". An example of a down-chirped pulse is shown in Fig. 1.4(c). Experiments and theoretical studies on coherent control of ultrafast electron dynamics by intense chirped laser pulses will be discussed in Secs. 1.3.2.3 and 1.3.3.2.

1.3 Phase Control on Model Systems

We now turn to the topic of coherent control. As described in the introduction the physical basis of coherent control is the manipulation of the interferences of matter waves. Effective tools to steer quantum wave packets are tailored ultrashort laser pulses, suitably adapted to the induced quantum dynamics. In particular, efficient control of coherently driven charge oscillations is enabled by the use of intense shaped femtosecond laser pulses. Coherent charge dynamics arise from the efficient light-induced superposition of non-degenerate bare quantum states. As such they are no longer eigenstates of the (interacting) system. A more natural description of coherent charge dynamics is provided by the dressed state picture. Therefore efficient manipulation of ultrafast laser-induced electron dynamics is based on the control of dressed states. This section aims to derive the basic physical concepts behind dressed state control. In a nutshell, the key to the control of dressed states (resonant AC Stark control) is the energy optimization of the laser-induced dipole, interacting with the external driving laser field, by tailoring the optical phase to the induced dipole dynamics. In order to gain intuition of how such an

optimization of the interaction energy is accomplished, we start with a simple classical model describing the laser-molecule interaction by a harmonic dipole oscillator driven on resonance by the electric field of an intense shaped laser pulse. Subsequently we model the strong-field driven electron dynamics quantum mechanically employing a two-state model interacting non-perturbatively with a resonant shaped femtosecond laser pulse. Here we derive rigorous conditions for the Selective Population Of Dressed States (SPODS) and discuss different physical mechanism to implement SPODS. Finally, we present applications of SPODS to the ultrafast efficient switching of photoexcitation in a multi-state model system.

1.3.1 Classical Model

We start our discussion of laser controlled electron dynamics in an intuitive classical picture. Reminiscent of the Lorentz model [90, 91], which describes the electron dynamics with respect to the nuclei of a molecule as simple harmonic oscillations, we consider the electron system bound to the nuclei as a classical harmonic oscillator of resonance frequency ω_r. Because the energies $\hbar\omega_r$ of electronic resonances in molecules are typically of the order $1-10$ eV the natural time-scale of the electron dynamics is a few femtoseconds to several hundred attoseconds. The oscillator is driven by a linearly polarized shaped femtosecond laser pulse $E_{\mathrm{mod}}(t)$ (see Eq. (1.8)). In order to elucidate the physical mechanism behind SPODS, i.e. the resonant control of coherent electron dynamics, the carrier frequency ω_0 of the pulse is tuned to the electronic resonance, $\omega_0 = \omega_r$. From a classical perspective the rapidly varying laser field distorts the outer electron shell and induces a coherent charge oscillation described by an oscillating electric dipole-moment $\mu(t)$. Phenomenologically the induced dipole is expressed by the (constant) polarizability $\hat{\alpha}$ of the molecule as $\mu(t) = \hat{\alpha} E_{\mathrm{mod}}(t)$. Here we pursue a more general approach in order to explicitly account for complex phase dynamics of the laser-dipole interaction. To this end we resort to the equation of motion

$$\ddot{\mu} + \omega_0^2 \mu = \frac{e^2}{m_e} E_{\mathrm{mod}}(t) \tag{1.18}$$

for a single valence electron of charge $-e$ and mass m_e. Damping mechanisms, such as spontaneous decay or collisional decoherence, may be disregarded on the femtosecond time-scale. With the Green function of the problem

$$G(t,t') = \frac{1}{\omega_0} \sin[\omega_0 (t-t')]\, \theta(t-t'), \tag{1.19}$$

where $\theta(t)$ is the Heavyside step-function, the solution of Eq. (1.18) for any shaped laser pulse $E_{\mathrm{mod}}(t)$ can be written as

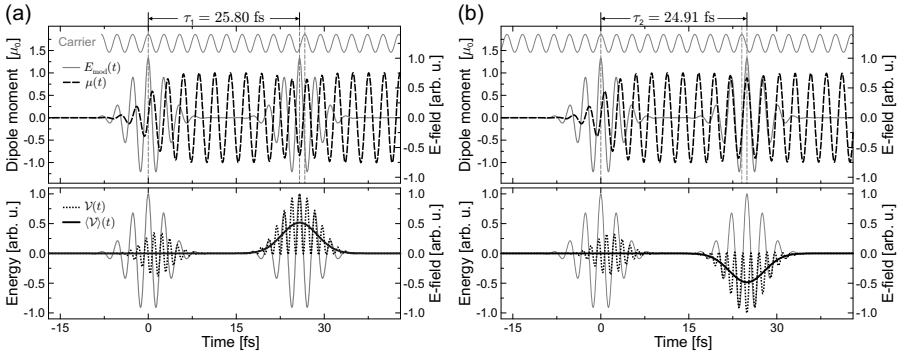

Figure 1.5 Dynamics of a classical electric dipole induced and driven on resonance by a sequence of two phase-locked ultrashort laser pulses. The driving laser field is shown as grey solid lines in all frames. In addition, the top frames show the induced dipole oscillation $\mu(t)$ as a black dashed line. The instantaneous interaction energy $\mathcal{V}(t)$ of the induced dipole in the external driving field is shown in the bottom frames as a black dotted line. Bold black lines display the time-average of the interaction energy $\langle\mathcal{V}\rangle(t)$. In (a) the phase relation between both pulses is desgined such, that the second pulse couples in anti-phase to the dipole oscillation induced by the first pulse. This leads to the maximization of the interaction energy. In (b) the second pulse is precisely timed to oscillate in phase with the induced dipole. As a result the interaction energy is minimzed.

$$\mu(t) = \frac{e^2}{m_e\omega_0} \int_{-\infty}^{t} E_{\mathrm{mod}}(t')\sin[\omega_0(t-t')]dt'. \tag{1.20}$$

Here we assumed the natural initial conditions $\mu(-\infty) = \dot{\mu}(-\infty) = 0$. Eq. (1.20) captures the full dependence of the induced dipole on the shaped laser field: $\mu(t) = \mu\left[E_{\mathrm{mod}}(t)\right](t)$. After evaluation of this expression the (instantaneous) interaction energy $\mathcal{V}(t)$ of the induced dipole in the external driving field is given by

$$\mathcal{V}(t) = -\mu(t) \cdot E_{\mathrm{mod}}(t). \tag{1.21}$$

Next we discuss a specific scenario based on a sequence of two phase-locked ultrashort laser pulses. Both pulses have a Gaussian-shaped envelope $\mathcal{E}_G(t)$ (cf. Eq. (1.12)) and are well-separated in time by a delay τ:

$$E_{\mathrm{mod}}(t;\tau) = \mathcal{E}_G(t)\cos(\omega_0 t) + \mathcal{E}_G(t-\tau)\cos[\omega_0(t-\tau)]. \tag{1.22}$$

The temporal dynamics of the molecular electric dipole excited by the pulse sequence is shown in Fig. 1.5(a) and (b) for two distinct values of τ. The respective upper frames show the induced dipole oscillation $\mu(t)$ (black dashed line) along with the driving electric field $E_{\mathrm{mod}}(t;\tau)$ (grey solid line), the lower frames display the corresponding interaction energy $\mathcal{V}(t)$ (black

dotted line) and its time-average $\langle \mathcal{V} \rangle(t)$ (bold black line). During the first pulse centered around $t = 0$ the solution in Eq. (1.20) takes the (approximate) form

$$\mu(t) \approx \frac{\mu_0}{2} \operatorname{Erfc}\left(-\frac{t}{\Delta t}\right) \sin(\omega_0 t), \tag{1.23}$$

with $\mu_0 = \sqrt{\frac{\pi}{8\ln(2)}} \frac{e^2 \Delta t}{m_e \omega_0} \mathcal{E}_0$ and Erfc being the complementary error-function. According to Eq. (1.23) the laser-driven dipole oscillation builds up sigmoidally and follows the driving laser field in quadrature, due to the resonant excitation. In this phase configuration the interaction energy $\mathcal{V}(t)$ (cf. Eq. (1.21)) oscillates rapidly with twice the carrier frequency ω_0, assuming both positive and negative values and therefore vanishing on the time average. This is illustrated in Fig. 1.5(a) and (b) during the first pulse. During the second pulse centered around $t = \tau$, however, the field-dipole phase relation – and hence the interaction energy – is controlled precisely by the time-delay τ. In (a) the second pulse is advanced with respect to the carrier oscillation of the first, such that it couples exactly in anti-phase to the induced dipole oscillation. In this phase configuration $\mathcal{V}(t)$ is strictly positive. Its time-average $\langle \mathcal{V} \rangle(t)$ is maximized at each instant of time, i.e. the energy of the interacting system of laser and molecule is maximized. This is the signature for the selective population of the upper dressed state in a quantum mechanical framework, as will be discussed in the following section. Vice versa, if the second pulse is retarded with respect to the carrier, such that it oscillates exactly in-phase with the induced dipole, the interaction energy is strictly negative as shown in (b). Here the energy of the interacting system is minimized at each time t, which corresponds to the selective population of the lower dressed state in the quantum mechanical picture.

The classical model discussed above is educative but simple. Basic aspects of strong-field control, e.g. the modification and coherent manipulation of the interaction energy stored in the laser-induced dipole dynamics, are intuitively captured, whereas other essential strong-field characteristics like population inversion or Rabi cycling are not adequately described. Hence, refined models are required for a more realistic description of the laser-initiated charge dynamics in molecules. In the next section we turn to a quantum mechanical treatment of the laser-matter-interaction and devise strategies for the efficient control of coherent electron dynamics by solving the Time-Dependent Schrödinger Equation (TDSE).

1.3.2 Selective Population of Dressed States

Next we model the laser-driven electron dynamics quantum mechanically to reveal analogies and differences to the simple classical model. In view of the SPODS-mechanism, which is based on resonant interactions, we consider only two quantum states at first, the ground state and the resonantly excited state.

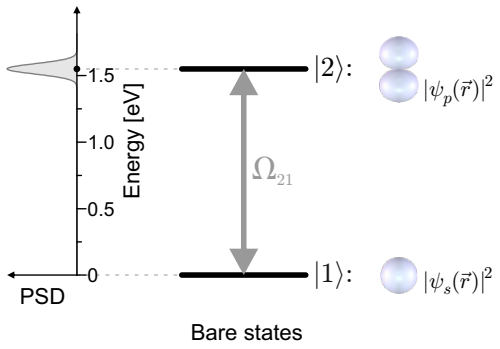

Figure 1.6 Two-state quantum system driven on resonance by an intense ultrashort (broadband) laser pulse. The Power Spectral Density (PSD) is plotted on the left-hand side. The ground state $|1\rangle$ is assumed to have s-symmetry as indicated by the spherically symmetric spatial electron distribution on the right-hand side. The excited state $|2\rangle$ is a p-state allowing for electric dipole transitions. Both states are coupled by the dipole matrix element μ_{21}. The dipole coupling between the shaped laser field and the system is described by the Rabi frequency $\Omega_{21}(t) = \mu_{21} E_{\mathrm{mod}}(t)/\hbar$.

For this purpose we briefly recapitulate the relevant equations for a two-state system driven on resonance by an intense shaped femtosecond laser pulse as described by Eqns. (1.6) and (1.8). The aim of this section is to build a bridge between the laser-dressed states of the system and the spatiotemporal dynamics of the electric dipole induced by – and simultaneously interacting with – the external laser field. Building on this relation we discuss two basic physical mechanisms to control the dressed state populations and verify, that the key to the realization of SPODS is the optimization of the interaction energy stored in the laser-induced charge oscillation.

1.3.2.1 Theoretical Framework We consider a one-electron quantum system of two states $|1\rangle$ and $|2\rangle$ with energies $\hbar\omega_1 = 0$ and $\hbar\omega_2 = 1.55$ eV (800 nm), coupled by an intense resonant ultrashort laser pulse $E_{\mathrm{mod}}(t)$. The system is illustrated in Fig. 1.6. The electron in state $|1\rangle$ and $|2\rangle$ is described by an s-wave $\psi_s(\boldsymbol{r})$ and a p-wave $\psi_p(\boldsymbol{r})$, respectively. The general time-dependent state of the electron interacting with the laser may then be expanded as

$$\psi(\boldsymbol{r},t) = c_1(t)\psi_s(\boldsymbol{r}) + c_2(t)\psi_p(\boldsymbol{r}). \tag{1.24}$$

The modulus square of the amplitudes $c_n(t)$ are the populations of the two states, $p_n(t) = |c_n(t)|^2$, i.e. the probabilities to find the electron in state $|n\rangle$ after time t. The time evolution of the electron in the external laser field is governed by the Time-Dependent Schrödinger Equation (TDSE)

$$i\hbar\frac{\partial}{\partial t}\psi(\boldsymbol{r},t) = \hat{\mathcal{H}}(t)\psi(\boldsymbol{r},t). \tag{1.25}$$

The total Hamiltonian reads $\hat{\mathcal{H}}(t) = \hat{\mathcal{H}}_0 + \hat{\mathcal{V}}(t)$, where $\hat{\mathcal{H}}_0$ is the time-independent Hamiltonian of the unperturbed system and $\hat{\mathcal{V}}(t)$ is the interaction describing the coupling between field and electron. In the dipole approximation this coupling is given by $\hat{\mathcal{V}}(t) = -\hat{\mu}_z E_{\mathrm{mod}}(t)$, if we assume the laser to be linearly polarized in z-direction and $\hat{\mu}_z = -ez$ is the component of the dipole operator parallel to the laser polarization. Inserting the expansion Eq. (1.24) into the TDSE (1.25) and projecting the result on states $|1\rangle$ and $|2\rangle$, respectively, yields the Schrödinger equation for the amplitudes $c_n(t)$ [92]:

$$i\hbar \frac{d}{dt} \begin{bmatrix} c_1 \\ c_2 \end{bmatrix} = \hbar \begin{bmatrix} 0 & -\Omega_{21}^*(t) \\ -\Omega_{21}(t) & \omega_2 \end{bmatrix} \begin{bmatrix} c_1 \\ c_2 \end{bmatrix}. \tag{1.26}$$

Here we introduced the Rabi frequency $\Omega_{21}(t)$ defined by the relation $\hbar\Omega_{21}(t) = \mu_{21} E_{\mathrm{mod}}(t)$, with the dipole matrix element $\mu_{21} = \langle 2|\hat{\mu}_z|1\rangle = -e\int_V \psi_p^*(\boldsymbol{r})\, z\, \psi_s(\boldsymbol{r}) d\boldsymbol{r}$. Eq. (1.26) is the TDSE in the Schrödinger picture. In general it proves more convenient to discuss the time-evolution of the driven system in a rotating frame, such as the frame rotating with the laser carrier frequency ω_0. After transformation into the carrier frequency picture and application of the Rotating Wave Approximation (RWA), the TDSE takes the form [92]

$$i\hbar \frac{d}{dt} \begin{bmatrix} c_1 \\ c_2 \end{bmatrix} = -\frac{\hbar}{2} \begin{bmatrix} 0 & \Omega_{21}^+(t) \\ \Omega_{21}^-(t) & 2\delta \end{bmatrix} \begin{bmatrix} c_1 \\ c_2 \end{bmatrix}. \tag{1.27}$$

Herein $\hbar\Omega_{21}^+(t) = \mu_{21}\mathcal{E}_{\mathrm{mod}}^+(t)$ is the complex-valued envelope of the Rabi frequency (cf. Eq. (1.6)) and $\hbar\Omega_{21}^-(t) = \left[\hbar\Omega_{21}^+(t)\right]^*$. The static detuning $\delta = \omega_0 - \omega_2$ was introduced only for completeness; throughout this manuscript we consider exact resonant excitation, i.e. $\delta = 0$. In general, the analytical integration of Eq. (1.27) for arbitrary pulse shapes $\mathcal{E}_{\mathrm{mod}}^+(t)$ is not feasible. Therefore the TDSE is solved numerically on a discrete time-grid using short-time propagator techniques [12]. By this means we obtain the quantum dynamics $\boldsymbol{c}(t) = [c_1(t), c_2(t)]^T$ in the bare state picture as a function of the applied laser pulse $\mathcal{E}_{\mathrm{mod}}^+(t)$.
In order to access the dressed states the Hamiltonian matrix

$$\mathcal{H}(t) = -\frac{\hbar}{2} \begin{bmatrix} 0 & \Omega_{21}^+(t) \\ \Omega_{21}^-(t) & 2\delta \end{bmatrix} \tag{1.28}$$

is diagonalized by the unitary transformation

$$\mathcal{U}(t) = \begin{bmatrix} \sin(\Theta) e^{i\zeta/2} & -\cos(\Theta) e^{i\zeta/2} \\ \cos(\Theta) e^{-i\zeta/2} & \sin(\Theta) e^{-i\zeta/2} \end{bmatrix}. \tag{1.29}$$

Here we introduced the mixing-angle $\Theta(t)$ defined by $\tan[2\Theta(t)] = \Omega_{\mathrm{mod}}(t)/\delta$ and $\Omega_{\mathrm{mod}}(t) = \left|\Omega_{21}^{\pm}(t)\right|$. The Hamiltonian in diagonal form reads

$$\mathcal{D}(t) = \mathcal{U}^\dagger \mathcal{H} \mathcal{U} = -\frac{\hbar}{2} \begin{bmatrix} \delta + \sqrt{\delta^2 + \Omega_{\mathrm{mod}}^2(t)} & 0 \\ 0 & \delta - \sqrt{\delta^2 + \Omega_{\mathrm{mod}}^2(t)} \end{bmatrix}. \tag{1.30}$$

The new diagonal elements are the eigenenergies $\varepsilon_l(t)$ and $\varepsilon_u(t)$ of the lower and upper dressed state $|l\rangle$ and $|u\rangle$, respectively. In intense laser fields the dressed states split up according to

$$\Delta\varepsilon(t) = \varepsilon_u(t) - \varepsilon_l(t) = \hbar\sqrt{\delta^2 + \Omega_{\mathrm{mod}}^2(t)} \tag{1.31}$$

For resonant excitation, $\delta = 0$, the splitting is determined only by the amplitude of the Rabi frequency which is conveniently adjusted via the laser field amplitude. Finally, we obtain the population dynamics $\boldsymbol{d}(t) = [d_l(t), d_u(t)]^T$ in the dressed state picture from the bare state amplitudes by the transformation $\boldsymbol{d}(t) = \mathcal{U}^\dagger(t)\boldsymbol{c}(t)$.
In order to relate the dressed state population dynamics to the more intuitive semiclassical picture of a laser-driven charge oscillation, we analyze the induced dipole-moment $\langle\mu\rangle(t)$ and the interaction energy $\langle\mathcal{V}\rangle(t)$ of the dipole in the external field. To this end we insert the solution of the TDSE (1.27) into the expansion of the wavefunction Eq. (1.24) and determine the time-evolution of the charge density distribution $\rho(\boldsymbol{r},t) = -e\,|\psi(\boldsymbol{r},t)|^2$ in space. From the density we calculate the expectation value of the dipole operator

$$\langle\mu\rangle(t) = \int_V \psi^*(\boldsymbol{r},t)\hat{\mu}_z\psi(\boldsymbol{r},t)dV = \int_V z\rho(\boldsymbol{r},t)dV = \mu_{21}\left[c_1(t)c_2^*(t) + c_1^*(t)c_2(t)\right]. \tag{1.32}$$

Again we note that – through the bare state amplitudes $c_n(t)$ – the induced dipole is a functional of the driving laser field: $\langle\mu\rangle(t) = \langle\mu\rangle\left[E_{\mathrm{mod}}(t)\right](t)$. The expectation value of the interaction energy is then given by the product

$$\langle\mathcal{V}\rangle(t) = \int_V \psi^*(\boldsymbol{r},t)\mathcal{V}(t)\psi(\boldsymbol{r},t)dV = -\langle\mu\rangle(t)\cdot E_{\mathrm{mod}}(t). \tag{1.33}$$

Applying the RWA, this expression reduces to $\langle\mathcal{V}\rangle(t) = -\langle\mu\rangle(t)\cdot\left|\mathcal{E}_{\mathrm{mod}}^+(t)\right|$. In the resonant case ($\delta = 0$) we furthermore have $\langle\mathcal{V}\rangle(t) = \langle\mathcal{H}\rangle(t) = \langle\mathcal{D}\rangle(t)$, where the second step follows from the invariance of the expectation values under unitary transformations. Thus, using Eq. (1.30) we find

$$-\langle\mu\rangle(t)\cdot\left|\mathcal{E}_{\mathrm{mod}}^+(t)\right| = \frac{1}{2}\hbar\Omega_{\mathrm{mod}}(t)\cdot\left[|d_u(t)|^2 - |d_l(t)|^2\right]. \tag{1.34}$$

Eq. (1.34) directly relates the energy stored in the laser-induced dipole oscillation to the energies ($\pm 1/2\hbar\Omega_{\mathrm{mod}}(t)$) and populations ($|d_n(t)|^2$) of the dressed states. It follows that the selective population of the upper (lower)

dressed state is equivalent to the maximization (minimization) of $\langle \mathcal{V} \rangle(t)$. The necessary condition for such an optimization of the interaction energy is the excitation of a dipole $\langle \mu \rangle(t)$ oscillating at maximum amplitude, i.e. the preparation of the system in a state of maximum electronic coherence, by the first part of the laser pulse. If this initial excitation is realized on resonance, the induced dipole oscillates in quadrature with the laser field in full analogy to the classical driven dipole discussed in Sec. 1.3.1. As a consequence the interaction energy, i.e. the left-hand side of Eq. (1.34), vanishes which in turn indicates a lack of selectivity among the dressed states: $|d_u(t)|^2 = |d_l(t)|$. Selection of a single dressed state is then accomplished by appropriate temporal phase matching between induced dipole and driving laser pulse: Aligning $\langle \mu \rangle(t)$ and $\left|\mathcal{E}^+_{\mathrm{mod}}(t)\right|$ in parallel configuration (phase-shift of 0) selects the lower dressed state, whereas anti-alignment of both (phase-shift of π) selects the upper. In an isolated two-state system these extreme configurations are considered to be immaterial [93]. However, when more states are involved, e.g. continuum states [68] or bound states [73], this bidirectional Stark shift is the essence of the described SPODS control scenario.

In the following we will discuss two basic – and in a sense complementary [44] – physical mechanisms to exert efficient control on the strong-field induced coherent electron dynamics. In the first scenario SPODS is implemented by a sequence of ultrashort laser pulses (discrete temporal phase jumps), whereas the second scenario utilizes a single chirped pulse (continuous phase variations) to exert control on the dressed state populations. Both mechanisms have distinct properties with respect to multi-state excitations such as those discussed in Sec. 1.3.3.

1.3.2.2 Photon Locking The first SPODS mechanism to be discussed is Photon Locking (PL) [94, 95, 93, 78], the optical analogue of the spin locking technique known from NMR [96]. PL is based on impulsive excitations by sequences of ultrashort laser pulses with discrete temporal phase jumps. The underlying physical mechanism was discussed in terms of the bare states [46, 78, 67], the dressed states [46, 68, 78] and the Bloch vector [79]. In Fig. 1.7(a) we illustrate the resonant interaction of the two-state system with a sequence of two 800 nm, 5 fs FWHM laser pulses. The real-valued laser field $E_{\mathrm{mod}}(t)$ is shown in frame (i). Frame (ii) displays the population dynamics of the ground state $|1\rangle$ (black dashed line) and excited state $|2\rangle$ (grey dashed-dotted line) along with the populations of the lower dressed state $|l\rangle$ (black solid line) and upper dressed state $|u\rangle$ (grey solid line), all of which are calculated in RWA. The induced dipole $\langle \mu \rangle(t)$ shown in frame (iii) (black dashed line) and the interaction energy $\langle \mathcal{V} \rangle(t)$ in frame (iv) (black dotted line) are calculated in the Schrödinger picture, in order to relate to the classical case discussed in Sec. 1.3.1. Also, the phase relation between induced dipole and driving laser field (grey solid line in (iii) and (iv)) becomes more transparent in the static, i.e., not rotating reference frame. For comparison, frame (iv) displays the RWA eigenenergies $\varepsilon_l(t)$ (black dashed-dotted line) and $\varepsilon_u(t)$

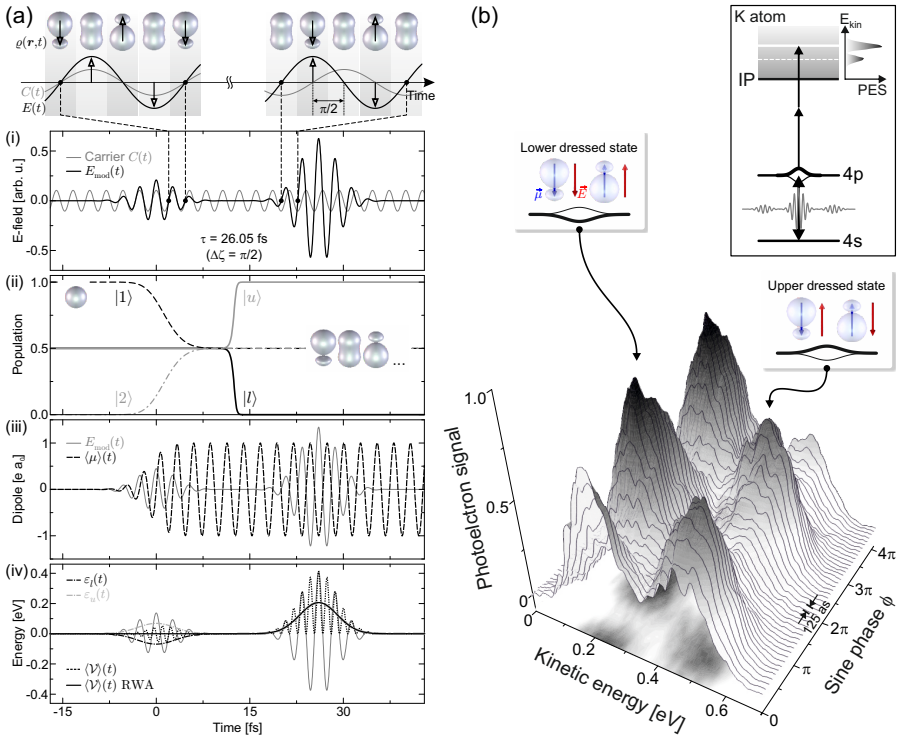

Figure 1.7 Photon Locking in a resonantly excited two-state system. (a) Numerical simulation results based on a sequence of two 800 nm, 5 fs FWHM laser pulses plotted in frame (i). Frame (ii) shows the time-evolution of the bare state (black dashed and grey dashed-dotted line) and the dressed state populations (black and grey solid line) in the RWA. The induced dipole dynamics, calculated in the Schrödinger picture, are displayed in frame (iii) as a black dashed line. The corresponding interaction energy of the dipole in the external field is plotted in frame (iv) as a black dotted line, and in RWA as a solid black line. For comparison the dressed state eigenenergies are shown as black and grey dashed-dotted lines. Snapshots of the induced spatiotemporal electron dynamics are shown on top of the figure. (b) Experimental results from strong-field excitation/ionization of K atoms (see inset) with multi-pulse sequences from sinusoidal spectral phase-modulation. The measured photoelectron spectra indicate efficient switching between the dressed states as a function of the sine parameter ϕ [68].

(grey dashed-dotted line) of the lower and upper dressed state. In addition, the interaction energy calculated in the RWA (black solid line) is shown. Finally, snapshots of the spatiotemporal electron density dynamics $\varrho(\boldsymbol{r},t)$ are shown on top of Fig. 1.7(a) to visualize the induced charge oscillation and its phase relation to the driving laser field.

The process starts in the ground state where the electron is described by an s-wave. For this highly symmetric charge distribution the dipole-moment, and hence the interaction energy, vanishes exactly indicating equal population of

the dressed states. The weak pre-pulse serves to launch the coherent charge oscillation. Designed with a pulse area [92] of

$$\theta_{\mathrm{pre}} = \int_{-\infty}^{\infty} \Omega_{\mathrm{pre}}(t)dt \stackrel{!}{=} \frac{\pi}{2} \tag{1.35}$$

it prepares the system in a state of maximum electronic coherence. The oscillating electron density is illustrated on top of the figure. During its preparation the induced dipole follows the driving field with a phase shift of $-\pi/2$ characteristic for resonant excitation. This results in fast ($2\omega_0$) bidirectional oscillations of the interaction energy with no net-effect on the time-average. Hence no selectivity among the dressed states is achieved yet, and both remain equally populated throughout the pre-pulse around $t = 0$. However, this changes dramatically with the onset of the main pulse. By virtue of a $+\pi/2$ phase-shift with respect to the pre-pulse the main pulse adapts itself in anti-phase to the induced dipole dynamics. As a consequence the interaction energy is instantaneously maximized just as in the classical case (see Fig. 1.5(b)). From now on $\langle\mathcal{V}\rangle(t)$ is strictly positive and on the time-average coincides with the RWA eigenenergy $\varepsilon_u(t)$. This indicates the selective population of the upper dressed state which is in fact verified by the population dynamics in frame (*ii*) around $t = 15$ fs. The phase jump of the laser field switches the system abruptly into the upper dressed state which remains populated selectively throughout the main pulse. Remarkably, also the bare state populations and the dipole amplitude remain constant during the main pulse. Due to the anti-phase relation between field and dipole no further excitation energy can be exchanged between both, so that the populations are locked despite the presence of an intense resonant laser field. For this reason the scenario also was termed "Do Nothing Pulse" in the bare state description [92].

In PL switching from the upper to the lower dressed state is achieved by switching the relative phase between pre- and main pulse by half an optical cycle. This shifts the main pulse in-phase with the induced dipole, leading to the minimization of the interaction energy (see also Sec. 1.3.3.1). Fig. 1.7(b) shows an experimental implementation of SPODS realized via PL on K atoms, which serve as a prototype system for the analysis of strong-field control mechanisms. Shown are measured energy-resolved photoelectron spectra from resonant strong-field excitation and simultaneous two-photon-ionization using multi-pulse sequences from sinusoidal spectral phase-modulation (cf. Sec. 1.2.1) [68]. The excitation/ionization scheme is depicted in the inset and the experimental procedure will be described in Sec. 1.4. Under non-perturbative resonant excitation the $4p$-state splits up into two dressed states. The ionization field maps the dressed states into the photoionization continuum giving rise to two strong-field ionization channels which emerge as the Autler-Townes (AT) doublet in the photoelectron spectrum. In view of the general control scheme presented in Fig. 1.1, these ionization channels represent ionic target

states perturbatively coupled to the neutral resonant state $4p$. In the experiment, efficient control on the ionic target channels was exerted by variation of the sine-phase parameter ϕ. As discussed in Sec. 1.2.1, ϕ determines the relative temporal phase between the first pre-pulse and the intense main pulse of the multi-pulse sequence. Therefore, as ϕ scans through two optical cycles the photoelectrons switch back and forth between the fast and the slow ionization channel, reflecting the alternating selective population of the upper and lower dressed state. The step-size $\Delta\phi = 0.3$ rad chosen in this experiment corresponds to a timing-precision of the induced electron dynamics of 125 as. In Sec. 1.5.3 we report on experiments exploring the limits of the electronic response to changes of the optical phase. In these experiments a switching precision in the order of sub-10 as was demonstrated [8].
The realization of SPODS via PL, i.e. impulsive excitation and discrete temporal phase variations, benefits from high peak intensities inherent to short laser pulses. In view of multi-state excitation scenarios this enables highly efficient population transfer to the target states (see Sec. 1.3.3). Furthermore PL can be implemented on very short time-scales which is desirable in order to outperform rapid intra-molecular energy redistribution or decoherence processes. On the other hand, since PL is an impulsive scenario it is sensitive to pulse parameters such as detuning and intensity [44]. A robust realization of SPODS is achieved by the use of adiabatic techniques. The underlying physical mechanism will be discussed next.

1.3.2.3 Rapid Adiabatic Passage Sequences of laser pulses as discussed in the previous section provide an efficient and transparent way to realize SPODS 'step-by-step'. However, through the preparation step, i.e. the impulsive excitation of a state of maximum coherence, the PL scenario is inherently sensitive to intensity fluctuations. A complementary and particularly robust approach to implement SPODS is based on adiabatic interactions using pulses with slowly varying envelopes and continuous temporal phase variations [72]. The physical mechanism behind this approach is Rapid Adiabatic Passage (RAP) [48] typically implemented by frequency chirped laser pulses. Originating from NMR [97] RAP was demonstrated in the optical regime on atoms [86, 48, 3, 98, 72] and theoretically on molecules [99, 100], where recently RAP-like scenarios were demonstrated experimentally on molecules with the help of shaped femtosecond light fields [101]. Fig. 1.8(a) shows numerical results for resonant excitation of the two-state system with a linearly chirped femtosecond laser pulse. The assignment of quantities is the same as in Fig. 1.7(a). The up-chirped laser pulse shown in frame (i) is generated by quadratic spectral phase-modulation (cf. Sec. 1.2.2) of a 2 fs FWHM input pulse, using a spectral chirp parameter of $\phi_2 = 11.0$ fs^2. Due to the chirp the pulse is stretched in time to $\Delta t_{\mathrm{mod}} = 15.4$ fs (cf. Eq. (1.15)). Excitation of the system starting from the ground state gradually launches the coherent charge oscillation. Due to the positive frequency sweep, the pulse starts with a strong red-detuning with respect to the electronic resonance, $\Delta(t) < 0$. Analogous

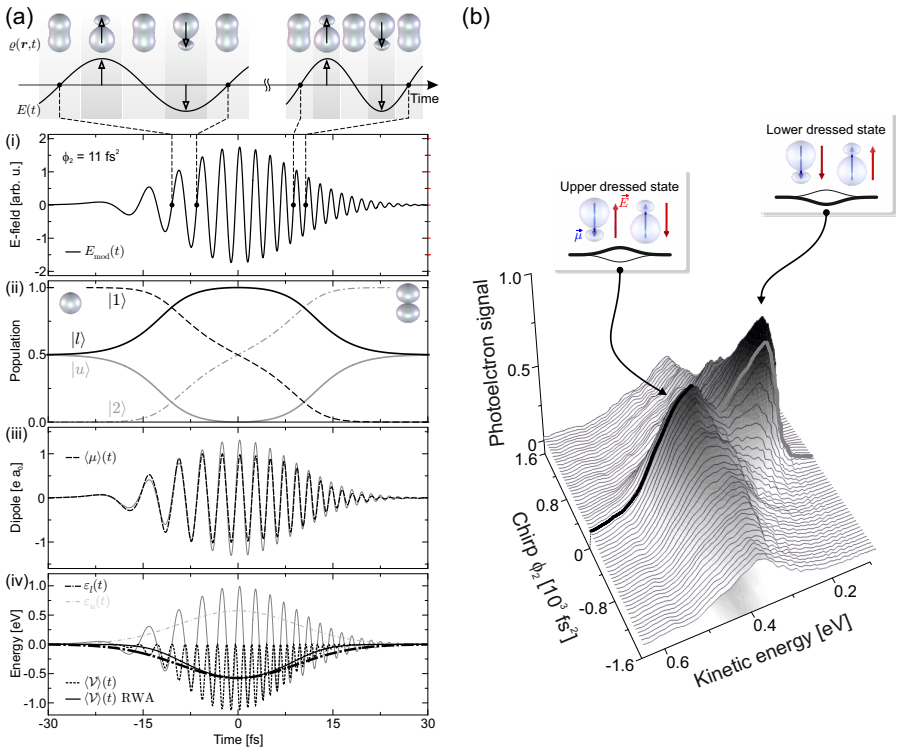

Figure 1.8 Rapid Adiabatic Passage in a resonantly driven two-state system. (a) Numerical simulation results based on a chirped 800 nm, 2 fs FWHM input pulse. For the assignment of quantities see Fig. 1.7. The up-chirped pulse is plotted in frame (i). Frame (ii) shows the time-evolution of the of the bare and dressed state populations in the RWA. The induced dipole dynamics displayed in frame (iii) are calculated in the Schrödinger picture. The corresponding interaction energy is plotted in frame (iv) along with the expectation value of the interaction operator in RWA and the dressed state eigenenergies. The top of the figure illustrates the induced spatiotemporal electron dynamics and their phase relation to the driving laser field. (b) Experimental results from strong-field excitation/ionization of K atoms with chirped pulses from quadratic spectral phase-modulation. The measured photoelectron spectra indicate efficient switching between the dressed states as a function of the chirp parameter ϕ_2 [72]. The bold line indicates the symmetric AT spectrum produced by the unchirped pulse.

to a classical oscillator driven below resonance the system follows the driving field strictly in-phase right from the beginning. Because both the amplitude and the detuning of the chirped pulse evolve sufficiently slow in time, the induced dipole is able to adapt to the field variations instantaneously. Due to this adiabatic following, the initial phase relation between field and dipole is maintained throughout the entire interaction. Thus under adiabatic conditions the phase matching of dipole and field is automatically fulfilled. As the dipole gains amplitude the interaction energy in frame (iv) is successively

lowered and the equal population of dressed states is lifted in favour of the lower dressed state. However, full selectivity among the dressed states is not attained before a dipole oscillation of maximum amplitude is established. This occurs in a small time window around $t = 0$ where the bare states in frame (ii) approach the state of maximum electronic coherence. Here the interaction energy $\langle \mathcal{V} \rangle(t)$ is minimized. Its time-average transiently coincides with the RWA energy $\varepsilon_l(t)$ indicating the selective population of the lower dressed state. The latter is verified by the population dynamics in frame (ii) around $t = 0$. Subsequently the pulse continues to invert the bare state system, which is typical for RAP. Just like the ground-state the excited p-state exhibits no permanent dipole-moment. Therefore both $\langle \mu \rangle(t)$ and $\langle \mathcal{V} \rangle(t)$ converge back to zero as the system is steered adiabatically towards state $|2\rangle$. This indicates the successive loss of selectivity among the dressed states, which is in fact observed in frame (ii) for $t > 0$. By the end of the pulse both dressed states are again fully equalized.

Here, switching from the lower to the upper dressed state is achieved by inversion of the sign of the chirp. A down-chirped laser pulse initially drives the system above resonance. Hence, provided the interaction conditions are adiabatic, the induced dipole will follow the field in anti-phase leading to a transient maximization of the interaction energy once the excitation reaches the state of maximum coherence (see also Sec. 1.3.3.2). Fig. 1.8(b) shows an experimental demonstration of SPODS realized via RAP on K atoms [72]. Shown are measured photoelectron spectra as a function of the chirp parameter ϕ_2 from quadratic spectral phase-modulation (see Eq. (1.11)). For unchirped pulses, i.e. $\phi_2 = 0$, the spectrum exhibits a symmetric AT doublet (see bold line in Fig. 1.8(b)). As discussed in the previous section, resonant BWL pulses populate both dressed states in equal measure achieving no selectivity. For $\phi_2 \neq 0$ however, the symmetry of the AT doublet is broken. Up-chirped pulses with $\phi_2 > 0$ selectively address the low-energy ionization channel, while the high-energy channel is completely suppressed. This indicates the selective population of the lower dressed state in the neutral system. For down-chirped pulses, $\phi_2 < 0$, the picture is inverted. Here the low-energy channel is eliminated from the spectrum and the high-energy ionization channel is addressed selectively due to selective population of the upper dressed state in the neutral system. The observed overall decrease of the photoelectron yield for large chirp parameters $|\phi_2|$ results from the lowered peak intensity of the chirped laser pulses (see Fig. 1.4). This affects the efficiency of multi-photon processes (two-photon ionization in this case) which has consequences for multi-state excitations such as the one discussed in the following Sec. 1.3.3. To conclude, driving quantum systems adiabatically is a robust method to control the populations of dressed states and realize SPODS. Ultrafast switching in multi-state systems involving multi-photon processes however requires higher pulse energies as in comparable PL scenarios, in order to achieve the same efficiencies, i.e. product yields.

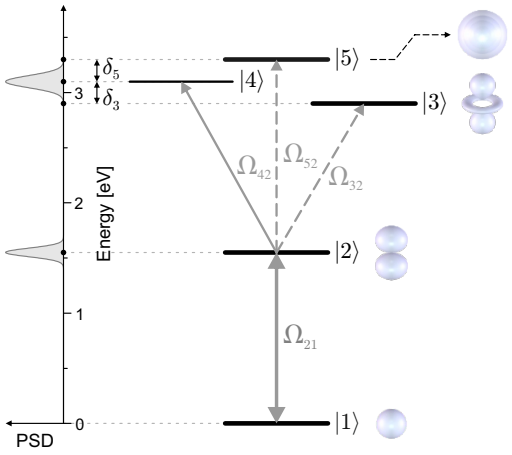

Figure 1.9 Generic five-state system for ultrafast efficient switching. The resonant two-state system of Fig. 1.6 is extended by three target states for selective excitation. While the intermediate target state $|4\rangle$ is in exact two-photon resonance with the laser pulse, both outer target states $|3\rangle$ and $|5\rangle$ lie well outside the bandwidth of the two-photon spectrum. Therefore these states are energetically inaccessible under weak-field excitation. Intense femtosecond laser pulses however utilize the resonant AC Stark effect to modify the energy landscape. As a result, new excitation pathways open up, enabling efficient population transfer to the outer target states as well.

1.3.3 Ultrafast Switching in Multi-State Systems

Efficient and selective excitation of electronic target states in atoms and molecules lies at the heart of photochemical applications (see corresponding references in Sec. 1.1) as well as quantum information processing [102, 103]. Here we demonstrate the potential of SPODS, introduced in the previous sections, for ultrafast electronic switching in a multi-state model system. In the previous Secs. 1.3.2.2 and 1.3.2.3 we already discussed two schemes for ultrafast switching among different target channels in the ionization continuum of K atoms. In these experiments the coupling between ionic target states and neutral system was perturbative since bound-ionic transitions are in general weak as compared to neutral transitions. However, the SPODS schemes discussed above are more general and remain valid even if the target states are not mere spectators of the resonantly driven sub-system. Below we present a fully non-perturbative treatment of the multi-state system shown in Fig. 1.9 exposed to intense femtosecond laser pulses, including the resonant AC-Stark shifts of all system states. We show that under such conditions the effective manipulation of the energy landscape in combination with precise phase control of the induced electron dynamics enables ultrafast switching between target states inaccessible in the weak-field regime, achieving unit efficiencies.

The system illustrated in Fig. 1.9 comprises a resonant sub-system $\{|1\rangle, |2\rangle\}$ and a set of high-lying target states $\{|3\rangle, |4\rangle, |5\rangle\}$ for selective excitation. All target states are coupled non-perturbatively to state $|2\rangle$ (coupling strength 1:4 with respect to μ_{21}). Note that the outer target states $|3\rangle$ and $|5\rangle$ lie well outside the bandwidth of the two-photon laser spectrum depicted on the left-hand side. The spectrum corresponds to an 800 nm, 20 fs FWHM input pulse. As a consequence only the two-photon resonant state $|4\rangle$ is accessible energetically in the weak-field regime. Intense resonant laser pulses on the other hand distort the systems energy landscape efficiently. The resonant AC Stark splitting induced in the resonant sub-system shifts the corresponding dressed states into resonance with states $|3\rangle$ and $|5\rangle$. By this means also the outer target states become accessible and are amenable for efficient population.

In the following Secs. 1.3.3.1 and 1.3.3.2 we discuss the selective excitation of the five-state system via PL and RAP, respectively. While PL, based on resonant interactions with constant instantaneous frequency, is most suitably described in the frame rotating with the laser carrier frequency ω_0, a description of adiabatic scenarios such as RAP, based on frequency-chirped pulses, is less transparent in this picture. For the discussion of the physical mechanism behind chirped excitation we change into the frame rotating with the instantaneous laser frequency $\omega_{\text{inst}}(t)$. In general, our analysis highlights the importance of choosing an appropriate reference frame for the analysis of basic strong-field control mechanisms.

1.3.3.1 Ultrafast Switching via PL In order to describe strong-field interaction of the five-state system in Fig. 1.9 with intense shaped femtosecond laser pulses the theoretical formalism prepared in Sec. 1.3.2.1 is readily extended. The RWA Hamiltonian $\mathcal{H}(t)$ for the five-state system in Fig. 1.9 in the frame rotating with the carrier frequency reads

$$\mathcal{H}(t) = -\frac{\hbar}{2}\begin{bmatrix} 0 & \Omega_{21}^{+}(t) & 0 & 0 & 0 \\ \Omega_{21}^{-}(t) & 0 & \Omega_{32}^{+}(t) & \Omega_{42}^{+}(t) & \Omega_{52}^{+}(t) \\ 0 & \Omega_{32}^{-}(t) & 2\delta_3 & 0 & 0 \\ 0 & \Omega_{42}^{-}(t) & 0 & 0 & 0 \\ 0 & \Omega_{52}^{-}(t) & 0 & 0 & 2\delta_5 \end{bmatrix}, \tag{1.36}$$

with $\hbar\delta_n = 2\hbar(\omega_0 - \omega_n) = \mp 200$ meV, for $n = 3, 5$. Fig. 1.10 presents numerical results for the excitation of the system with a resonant multi-pulse sequence from sinusoidal spectral phase-modulation (cf. Sec. 1.2.1) of an 800 nm, 20 fs FWHM input pulse. In Sec. 1.3.2.2 we exemplarily discussed the selective population of the upper dressed state $|u\rangle$ in a two-state system by this class of pulses. Here we deliberately chose the inverse scenario, i.e. selective population of the lower dressed state $|l\rangle$ of the resonant sub-system, and anticipate the efficient and selective excitation of the lower target state $|3\rangle$. The shaped laser pulse shown in Fig. 1.10(a) is the result of a complete

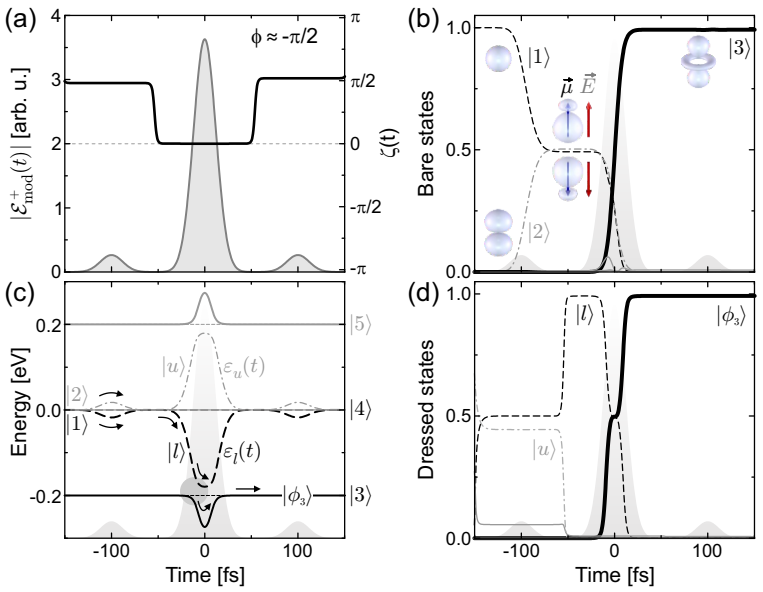

Figure 1.10 Ultrafast efficient switching in the five-state system via SPODS based on multi-pulse sequences from sinusoidal phase-modulation (PL). The shaped laser pulse shown in (a) results from complete forward design of the control field. Frame (b) shows the induced bare state population dynamics. After preparation of the resonant sub-system in a state of maximum electronic coherence by the pre-pulse, the optical phase-jump of $\Delta\zeta = -\pi/2$ shifts the main pulse in-phase with the induced charge oscillation. Therefore the interaction energy is minimized resulting in the selective population of the lower dressed state $|l\rangle$, as seen in the dressed state population dynamics in (d) around $t = -50$ fs. Due to the efficient energy splitting of the dressed states, induced in the resonant sub-system by the main pulse, the lower dressed state is shifted into resonance with the lower target state $|3\rangle$ (see frame (c) around $t = 0$). As a result, 100% of the population is transferred non-adiabatically to this particular target state, which is selectively populated by the end of the pulse.

forward design of the control field. By choice the sine-frequency $T = 100$ fs significantly exceeds the temporal FWHM $\Delta t = 20$ fs of the input pulse to ensure that all sub-pulses are well-separated in time. In order to address the lower dressed state $|l\rangle$, the sine-phase was set to $\phi = -\pi/2$ to introduce a phase-jump of $\Delta\zeta = -\pi/2$ between the first pre- and the main pulse, as discussed in 1.3.2.2. The total and relative amplitudes of the sub-pulses were adjusted via the sine-amplitude $A = 0.145$ and the input field amplitude $\mathcal{E}_0$, respectively. Both parameters were optimized following two conditions. The first requirement is to generate a pre-pulse with a pulse-area of (cf. Eqns. (1.10) and (1.35))

$$\theta_{\mathrm{pre}} = \frac{\mu_{21}}{\hbar} \cdot J_{-1}(A) \int_{-\infty}^{\infty} \mathcal{E}(t+T)dt \stackrel{!}{=} \frac{\pi}{2}. \tag{1.37}$$

The pre-pulse thus prepares the system in a state of maximum electronic coherence (see Fig. 1.10(b) around $t = -100$ fs). Only 0.5% of the population escapes to the resonant target state $|4\rangle$. Transitions to the off-resonant target states $|3\rangle$ and $|5\rangle$ are completely suppressed since the dynamic Stark splitting of the resonant sub-system induced by the pre-pulse is too small to overcome the energy gap of 200 meV. Because the electronic coherence is excited on resonance the induced dipole follows the field in quadrature. Therefore, lower and upper dressed state $|l\rangle$ and $|u\rangle$ are almost equally populated during the pre-pulse as shown in Fig. 1.10(d). The optical phase-jump between pre- and main pulse adapts the laser field to the induced charge oscillation. As a result of the $-\pi/2$-jump the onsetting main pulse is shifted in phase with the dipole, minimizes the interaction energy and selectively populates the lower dressed state $|l\rangle$ (see Fig. 1.10(d) at $t = -50$ fs). Proceeding along state $|l\rangle$ the system rapidly approaches the lower target state $|3\rangle$ (black arrows). With the Rabi frequency of the main pulse chosen to exceed the energy separation of the outer target states, $\hbar\Omega_{21}(0) > 400$ meV (cf. Sec. 1.5.1), two avoided crossings arise in Fig. 1.10(c) at $t = \mp 10$ fs between states $|l\rangle$ and $|\phi_3\rangle$, the first of which is marked by a grey circle. Due to the highly non-adiabatic time evolution diabatic transitions between these dressed states are likely to occur. The Landau-Zener model [104, 105, 48] estimates the probability for a diabatic transition at the avoided crossings as

$$p_{|l\rangle \to |\phi_3\rangle} \approx \exp\left[-2\pi\hbar \frac{\Omega_{32}^2}{|\sigma|}\right]. \tag{1.38}$$

Herein σ is the rate of change of the lower dressed state energy $\varepsilon_l(t)$ (black dashed line in Fig. 1.10(c)) evaluated at the inflection points at $t = \mp 15$ fs, and the Rabi frequency Ω_{32} is evaluated at the crossing times. For symmetry reasons the Landau-Zener probability is the same for both avoided crossings. Now the second requirement concerning the field amplitude is to tailor the Rabi frequency of the main pulse such that $p_{|l\rangle \to |\phi_3\rangle} = 0.5$. Then 50% of the population is transferred to state $|\phi_3\rangle$ at the first avoided crossing, the remaining 50% are transferred at the second. Since states $|\phi_3\rangle$ and $|3\rangle$ coincide once again after the interaction, eventually 100% of the population is transferred to the lower target state.

In order to switch the system into the upper target state $|5\rangle$ merely the sine-phase ϕ has to be varied by half an optical cycle, i.e. by $\Delta\phi = \pi$. In this case the main pulse is phase-shifted by $\Delta\zeta = +\pi/2$ with respect to the pre-pulse and couples in anti-phase to the induced charge oscillation. Hence the interaction energy is maximized and the upper dressed state $|u\rangle$ is populated selectively. Due to the energy increase the system rapidly approaches the

upper target state $|5\rangle$. The ensuing non-adiabatic transitions between the dressed states $|u\rangle$ and $|\phi_5\rangle$ result in a complete population transfer from the resonant sub-system to the upper target state, which is selectively excited by the end of the pulse.

1.3.3.2 Ultrafast Switching via RAP Next we employ chirped pulses and investigate the aspects of adiabatic time-evolution in the strong-field excitation of the five-state system of Fig. 1.9. Similar scenarios to invert multi-state systems using chirped pulses have been reported by various groups on atoms [86, 106, 48, 107, 108, 53] and molecules [100, 48]. While impulsive processes based on discrete temporal phase jumps but otherwise constant laser frequency are transparently described in the frame rotating with the carrier frequency ω_0, this picture is less suited whenever transient resonances due to time-varying laser frequencies play a role. Such dynamic resonances (level crossings) are the essence of adiabatic processes. Therefore adiabatic scenarios such as RAP are most suitably described in the frame rotating with the instantaneous laser frequency $\omega_{\mathrm{inst}}(t)$. In this picture the RWA Hamiltonian $\mathcal{H}(t)$ for the five-state system reads [92]

$$\mathcal{H}(t) = -\frac{\hbar}{2}\begin{bmatrix} 2\Delta_1(t) & \Omega_{21}(t) & 0 & 0 & 0 \\ \Omega_{21}(t) & 2\Delta_2(t) & \Omega_{32}(t) & \Omega_{42}(t) & \Omega_{52}(t) \\ 0 & \Omega_{32}(t) & -2\omega_3 & 0 & 0 \\ 0 & \Omega_{42}(t) & 0 & -2\omega_4 & 0 \\ 0 & \Omega_{52}(t) & 0 & 0 & -2\omega_5 \end{bmatrix}, \tag{1.39}$$

with $\Delta_1(t) = -2\omega_{\mathrm{inst}}(t)$ and $\Delta_2(t) = -\omega_{\mathrm{inst}}(t) - \omega_2$. The numerical results for strong-field excitation of the system with an intense chirped laser pulse are presented in Fig. 1.11. In contrast to Sec. 1.3.2.3, where we discussed the selective population of the lower dressed state $|l\rangle$ in a two-state system driven by an up-chirped pulse, here we describe the inverse scenario, i.e. selective population of the upper dressed state in the resonant sub-system by a down-chirped pulse, entailing selective excitation of the upper target state $|5\rangle$. The chirped laser pulse, as shown in Fig. 1.11(a) results from quadratic spectral phase-modulation (cf. Sec. 1.2.2) of the 800 nm, 20 fs FWHM input pulse with a chirp parameter of $\phi_2 = -2000$ fs^2. Due to the down-chirp, the chirped eigenenergy of the ground state $|1\rangle$ sweeps linearly across the target states, starting well above state $|5\rangle$ and generating a couple of dynamic resonances in the course of the interaction. The first crossing occurs in the rising edge of the pulse (see Fig. 1.11(c) around $t = -350$ fs). The light-induced coupling however is already strong enough and the frequency sweep is sufficiently slow to ensure adiabatic conditions [48]. As a result the system traverses the (avoided) crossing adiabatically, i.e. without undergoing a transition from the upper dressed state $|u\rangle$, initially associated with state $|1\rangle$, to the lower dressed state $|l\rangle$, initially associated with state $|2\rangle$. In the spatiotemporal dipole pic-

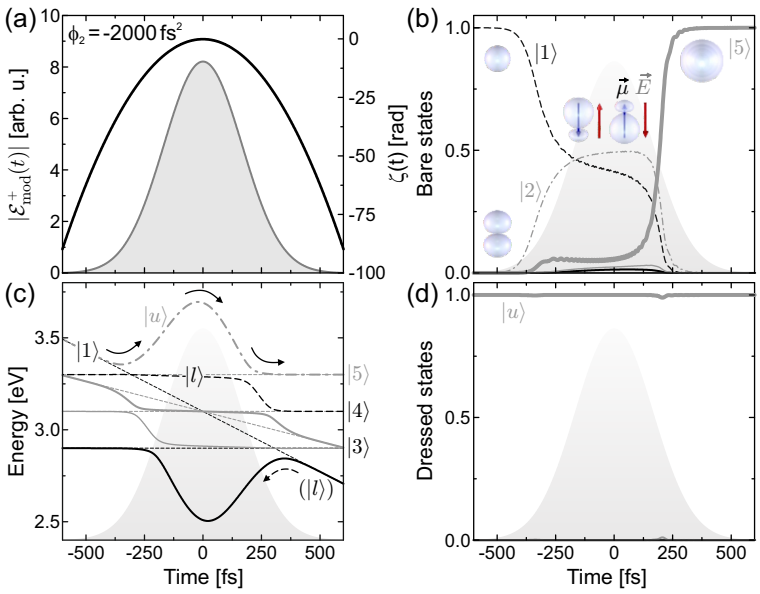

Figure 1.11 Ultrafast efficient switching in the five-state system via SPODS based on chirped pulses from quadratic phase-modulation (RAP). The down-chirped laser pulse is shown in frame (a). Frame (b) shows the induced bare state population dynamics. During the rising edge of the pulse the resonant sub-system is steered into a state of maximum electronic coherence. Due to the initial blue-detuning of the field with respect to the resonance, the induced charge oscillation adiabatically follows the driving field in anti-phase right from the beginning. The interaction energy is gradually maximized indicating the selective population of the upper dressed state $|u\rangle$. Verified by the dressed state population dynamics in (d) the upper dressed state is selectively populated throughout the entire interaction due to adiabatic interaction. As seen in the energy diagram in (c) the upper dressed, initially associated with the ground state $|1\rangle$, is subject to two avoided crossings with the lower dressed state $|l\rangle$ around $t = -350$ fs and $t = 200$ fs. As a consequence, it changes its association and finally coincides with state $|5\rangle$, which is selectively populated by the end of the pulse.

ture the rising edge of the pulse induces a coherent charge oscillation which follows the driving field adiabatically and, due to the initial blue-detuning, in anti-phase configuration. Hence the interaction energy is gradually increased as the dipole gains amplitude, i.e. as the resonant sub-system approaches the state of maximum coherence. Proceeding along the upper dressed state the system encounters a second avoided crossing with the lower dressed state in the trailing edge of the pulse around $t = 200$ fs. Again the time-evolution is adiabatic so that no diabatic transitions occur. However, here the upper dressed state changes its association. It approaches the upper target state $|5\rangle$ and by the time the interaction is over fully coincides with this particular target state. Eventually, 100% of the population is delivered adiabatically

from the ground state $|1\rangle$ to the target state $|5\rangle$ via selective population of the upper dressed state $|u\rangle$.
The inverse scenario, i.e. selective excitation of the lower target state $|3\rangle$, is achieved by flipping the sign of the chirp. Changing the chirp direction is equivalent to time reversal in the dressed state picture [48], i.e. of the energy and population dynamics shown in Fig. 1.11(c) and (d). The up-chirped ground state $|1\rangle$ starts below state $|3\rangle$ and sweeps linearly across the target states. Thus the system is initialized in the lower dressed state $|l\rangle$ which, under adiabatic conditions, remains populated selectively throughout the interaction. Following the above arguments the system is steered adiabatically from the ground state towards the lower target state $|3\rangle$, which is selectively excited by the end of the pulse.

1.4 Experimental Setup

In Sec. 1.3.2 we presented experimental data from strong-field excitation and ionization of K atoms with shaped femtosecond laser pulses. Here we give a description of the apparatus and strategy used in the experiments presented in this contribution. Fig. 1.12 gives an overview over the complete experimental two-color setup. For the experiments on strong-field control of K atoms (cf. Secs. 1.3.2.2, 1.3.2.3 and 1.5) only the one-color beamline was used. An amplified 1 kHz Ti:sapphire laser system provides intense 795 nm, 30 fs FWHM laser pulses which are referred to as infrared (IR) input pulses. The IR input pulses are spectrally phase-modulated by a home-built Fourier-transform pulse shaper based on a computer-controlled Liquid Crystal Spatial Light Modulator (LC SLM) in the Fourier plane of a $4f$-setup [109, 110, 8]. Application of the desired phase mask $\varphi(\omega)$ to the SLM yields shaped IR pump pulses at the output of the shaper. The shaped IR pump pulses are attenuated to pulse energies of about 0.1 to 2.0 μJ and focused into the interaction region of a Time-Of-Flight (TOF) photoelectron spectrometer. Here the laser beam intersects a supersonic potassium beam from an adjacent oven chamber. In the experiments on K_2 molecules (see Sec. 1.6) the particle beam is seeded with Ar gas to promote the dimer formation. Photoelectrons released during the strong-field interaction of shaped IR pulses with isolated K atoms or K_2 molecules in the beam are collected by a magnetic bottle and detected using a Multi Channel Plate (MCP) detector. After calibration of the spectrometer using different narrowband laser sources and buffer gases we obtain energy resolved photoelectron spectra which are studied as a function of the IR pulse shape, i.e. the applied phase mask $\varphi(\omega)$.

The figure of merit in the experiments on K atoms is the photoelectron yield in different ionization channels produced immediately by the shaped IR pump pulse (ultrafast switching between ionic target channels). This quantity is readily extracted from the measured photoelectron spectra. In the experiments on K_2 molecules however the objective is ultrafast switching in the

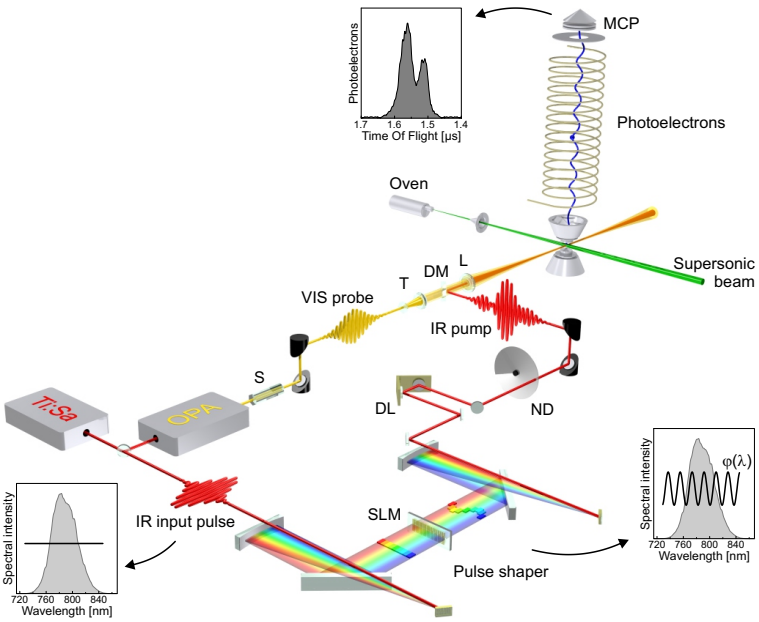

Figure 1.12 Experimental two-color setup featuring an IR beamline, to generate intense shaped IR pump pulses, and a VIS probe beamline, to provide time-delayed probe pulses of a different color. Both beams are focused collinearly into a supersonic beam to interact with isolated K atoms and molecules. Photoelectrons released during the interaction are measured by an energy-calibrated TOF-spectrometer. The following abbreviations are used: SLM: Spatial light modulator, DL: Delay line, ND: Continuous neutral density filter, L: Lens, S: Stretcher, T: Telescope, DM: Dichroic mirror, MCP: Multi channel plate detector.

neutral system. In order to probe the population of the neutral target states excited by the IR pump pulse we employ an Optical Parametric Amplifier (OPA), pumped by a fraction of the IR input pulse and operating at a central wavelength 570 nm. The visible (VIS) probe pulses are stretched in time to avoid direct multi-photon ionization as a background signal and, moreover, to average over the nuclear wavepacket dynamics launched in the target states, smoothing the photoelectron signals. Subsequently the probe beam is magnified by a telescope (magnification factor 2.7) and focused tightly into the center of the IR laser focus. By this means we prevent averaging over the focal intensity distribution of the IR pump laser which typically leads to a blurring of strong-field effects. A delay line in the IR one-color beamline serves to adjust the time-delay between the IR pump and the VIS probe pulse. Both beams are combined by a dichroic mirror and focused collinearly into the interaction region of the spectrometer.

In all experiments we start with an *in situ* compensation of the residual spec-

tral phase of the IR pump pulse, introduced by dispersive elements in the pump beamline. By this means we make sure to have BWL pulses in the experiment if the zero phase is applied to the SLM. The residual phase is found by adaptive optimization of the total photoelectron yield from multi-photon ionization of ground state Xe atoms which are led effusively into the interaction region. It turned out to be sufficient to parameterize the trial phase by a 5^{th} order polynomial. In the experiments the optimal result $\varphi_{\rm opt}(\omega)$ is always applied to the SLM in addition to the desired phase mask $\varphi(\omega)$.

1.5 Experimental Implementation

This section is dedicated to experimental studies on the strong-field control of coherent electron dynamics based on SPODS as discussed in Sec. 1.3.2. Again we use the K atom as a prototype of a two-state system interacting non-perturbatively with intense shaped femtosecond laser pulses. In Secs. 1.3.2.2 and 1.3.2.3 we already discussed efficient ultrafast switching among dressed states in K atoms via the strong-field control mechanisms of PL and RAP, respectively. Here we extend these studies and investigate in detail different aspects of SPODS realized by shaped femtosecond laser pulses. In Sec. 1.5.1 we study the tunability of the dressed state energies in order to address different target channels in multi-state systems. Sec. 1.5.2 describes an adaptive control approach to optimize the selectivity among the dressed states by allowing for more complex shaped pulses. Finally, in Sec. 1.5.3 we explore the limits of precision in the coherent control of the strong-field induced ultrafast electron dynamics.

1.5.1 Tunability

In the discussions above and the experiments presented so far (see Sec. 1.3.2) we exerted phase control to select a single dressed state at a given energy separation between both dressed states. In view of applications to quantum control, selectivity and efficient population transfer to specific target states are both important. The latter is achieved by tuning the dressed state energies into resonance with the (likewise dressed) target states. In this section we present our experimental results on the tunability of the dressed state energies by variation of the laser intensity. According to Eq. (1.31) the dressed state energy splitting in the resonant case is given by $\Delta\varepsilon(t) = \hbar\Omega(t)$ (the index 'mod' is dropped because we consider BWL pulses here). The Rabi frequency in this expression is proportional to the laser electric field $\mathcal{E}(t)$ which, in turn, is proportional to the square root of the laser intensity $I(t)$. Therefore we use the laser pulse energy W, being a measure for the laser intensity for a given pulse duration Δt and laser spot size, as a convenient experimental parameter to tune the energy of the dressed states. From these considerations we expect a square root dependence of the measured energy splitting with respect to the

pulse energy: $\hbar\Omega(t) \propto \sqrt{I(t)}$.
In the experiment we measured photoelectron spectra from strong-field excitation and simultaneous two-photon ionization of K atoms with BWL (unmodulated) IR pump pulses, as a function of the pulse energy W [68]. The results for energies ranging from $W = 0.35$ μJ to 2 μJ are shown in logarithmic representation in Fig. 1.13. All photoelectron spectra exhibit the AT doublet as a signature of the dressed states. The observed AT splittings $\hbar\Omega_0$ reflect the corresponding dressed state splittings $\Delta\varepsilon$ at the time of maximum laser intensity I_0. In this time window the two-photon ionization probability is highest and the majority of photoelectrons is born. In order to determine the AT energy splittings quantitatively the sum of two Gaussians was fitted to the measured spectra. The centers of both Gaussians are plotted as open circles on top of the spectra. The increase of the splitting with increasing laser pulse energy is visualized by grey dashed-dotted lines. The splitting of $\hbar\Omega_0 = 150$ meV at the lowest laser energy (0.35 μJ) and $\hbar\Omega_0 = 270$ meV at the highest laser energy (2 μJ) of our measurements is indicated with black bars. For comparison, the spectral bandwidth $\Delta\omega$ of the 30 fs FWHM IR input pulse ($\hbar\Delta\omega = 60$ meV) is also shown. In fact, the tunability achieved by strong-field control exceeds the laser bandwidth by a factor of 4.5. The inset to Fig. 1.13 shows a log-log plot of the energetic splitting $\hbar\Omega_0$ as a function of the laser pulse energy W. The observed energy dependence $\hbar\Omega_0 \propto W^{0.46\pm0.04}$ confirms the expected square root dependence. At energies around 2 μJ the curve starts to saturate because higher excited states of the potassium atom take part in the excitation process.

1.5.2 Selectvity

In addition to the control of dressed state populations based on the knowledge of physical mechanisms as discussed in Sec. 1.3.2, here we report on an experiment to study strong-field feedback optimization of SPODS. Quantum control by adaptive feedback controlled optimization has been proposed by Judson and Rabitz [34] and today been implemented in numerous experiments ranging from the control of atoms and molecules to the generation of optimized attosecond pulses (see Sec. 1.1 for corresponding references). In this section, we study the adaptive optimization of one AT component to optimize transient SPODS, i.e. SPODS during the most intense part of the shaped pulse. In the multi-pulse scenarios presented in Sec. 1.3.2.2, SPODS is realized during the intense main pulse with unit efficiency. However, ionization during the additional sub-pulses always provides a constant background of symmetric AT signal which cannot be controlled by the phase of the second pulse. Therefore, we investigate if complex pulses exist which optimize transient SPODS beyond the level of control achieved in multi-pulse experiments. The computer controlled LC SLM produces complex shaped femtosecond laser pulses from the initial BWL IR input pulse. We use a linear combination of the area

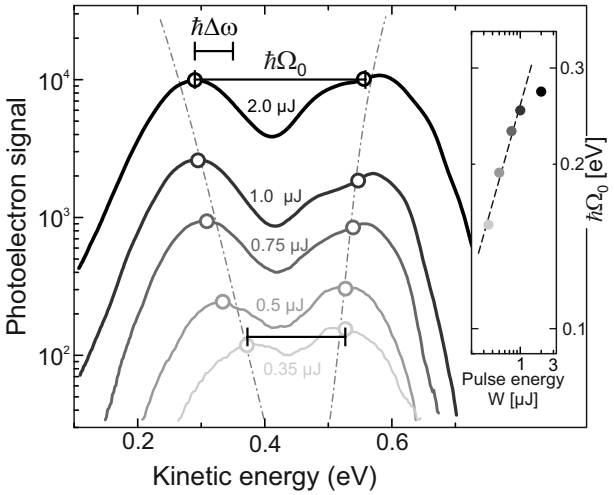

Figure 1.13 The energy tunability of the dressed states is demonstrated on the splitting $\Delta\varepsilon = \hbar\Omega_0$ of the photoelectron spectra as a function of laser energy W. For the lowest and highest laser energy the splitting is $\hbar\Omega_0 = 150$ meV and 270 meV, respectively (black bars). The spectral width $\hbar\Delta\omega$ of a 30 fs laser pulse (60 meV) is shown for comparison. Dashed-dotted lines indicate the trend of the splitting with increasing laser energy. The inset shows a log-log plot of $\hbar\Omega_0$ as a function of the pulse energy W. The observed slope of 0.46 ± 0.04 (dashed line) confirms that the splitting increases with the square root of the laser intensity I [68].

of the fast photoelectrons F and the area of the slow photoelectrons S (see Figure 1.14(a)) as the fitness value

$$f = 5 \cdot F - S \tag{1.40}$$

of each pulse shape to optimize one AT peak against the other and simultaneously obtain the highest possible absolute photoelectron yield. The fitness is optimized by the variation of the pulse shape using an evolutionary optimization algorithm. Consequently, the maximum attainable control in this scenario is the complete elimination of one AT component while enhancing the other. Fig. 1.14 shows the experimental photoelectron spectra during the adaptive optimization of the fast photoelectrons [78]. The reference photoelectron spectrum at the begin of the optimization procedure is depicted in Fig. 1.14(a). It is clearly seen, that the intensity of the fast photoelectrons rises with increasing number of iterations (b) - (d) beyond the initial intensity indicated by the bold lines. Simultaneously, the slow photoelectrons are significantly reduced in intensity compared to the reference indicated by the dashed line. Normalized to the reference values, the intensity ratio of the AT components – and hence the selectivity – has been increased by a factor of 6.

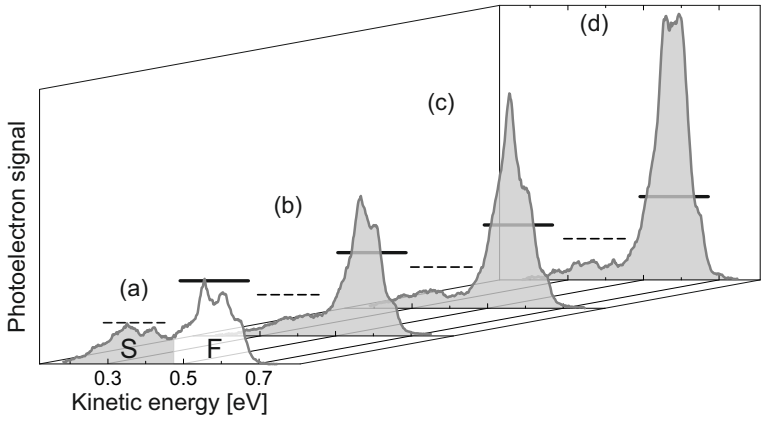

Figure 1.14 Evolution of the photoelectron spectra during the adaptive optimization of the fast versus the slow photoelectrons. The fitness function is defined as $f = 5F - S$, where F denotes the area of the fast photoelectrons (grey shaded) and S the area of slow photoelectrons. The number of iterations increases from (a) to (d). The horizontal lines indicate the reference intensities of the slow (dashed) and fast (bold) photoelectrons at the begin of the optimization procedure. The optimal pulse (d) realizes the population of the upper dressed state during ionization with supreme selectivity.

This result shows that by use of suitably shaped pulses transient SPODS can be realized with almost 100% efficiency.

1.5.3 Precision

Because electrons are much lighter than nuclei, they move much faster. The intrinsic temporal regime for valence bond electron dynamics is the few femtosecond to several hundred attosecond time-scale. Therefore efficient and accurate control of electron dynamics requires extreme precision regarding the control field. Commonly attosecond techniques are considered to be the appropriate tools for efficient manipulation of electron motions [111, 112, 61, 62, 63]. However attosecond pulses in the XUV region are not suited for efficient valence bond excitation (see Sec. 1.1). Here we demonstrate that ultrafast electron dynamics are controlled efficiently on the sub-10 as time-scale employing a pair of femtosecond laser pulses with a temporal separation controllable down to zeptosecond precision [8].
In Sec. 1.3.2 we used photoelectrons from simultaneous excitation and ionization of K atoms as an extremely sensitive probe for the coherent electronic dynamics driven in the neutral system. Differences of the electronic response to optical phase changes in the order of 100 as were readily observed in the experiment reported in Sec. 1.3.2.2. In order to explore the limits of the timing precision we repeated this experiment with successively increasing res-

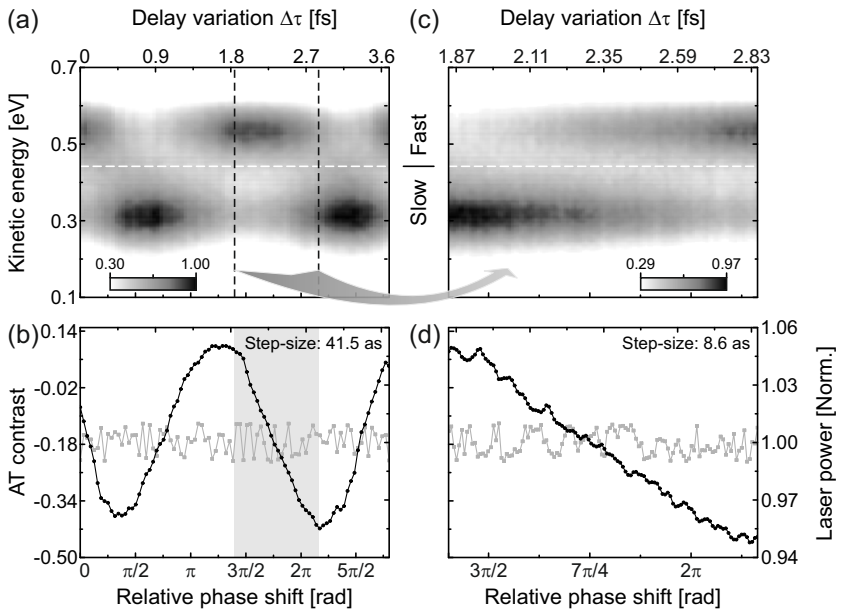

Figure 1.15 High-precision switching between dressed states in K atoms using a pair of precisely timed femtosecond laser pulses from an all-optical common-path interferometer. Upper panel: Photoelectron spectra recorded as a function of the pulse separation $\tau = \tau_0 + \Delta\tau$, with $\tau_0 = 120$ fs to ensure temporally separated pulses. The top axis indicates the delay variation $\Delta\tau$ while the bottom axis indicates the corresponding phase shift between the two pulses. Lower panel: AT contrast curves (black line), derived from the photoelectron spectra, to capture the electronic response to the optical phase changes in a scalar observable. In (a) and (b) the AT contrast behaves strictly monotonic as the photoelectrons switch from one channel to the other (see e.g. grey-shaded area) indicating the controllability of the underlying neutral electron dynamics on a temporal level of the step-size of 41.5 as. The experimental limit of controllability is sub-10 as. As demonstrated in (c) and (d) first deviations from monotony are detected when the step-size is decreased to 8.6 as. Note that the laser power (grey line) remains constant on a 1% level, underscoring the fact that the observed contrast variation is a pure phase effect resulting from coherent control of the induced electron dynamics.

olution, i.e. decreasing time steps. Instead of using multi-pulse sequences from sinusoidal phase-modulation however we utilized our pulse shaper as a high-precision common-path interferometer [113, 114] to generate pairs of precisely timed femtosecond laser pulses [8]. The shaper setup used as an all-optical interferometer is based on a dual-layer SLM, to individually modulate two orthogonal polarization components of the input pulse, and a polarizer to project both components onto the horizontal plane, providing linear polarization at the shaper output. Application of different linear spectral phases to both SLMs generates two time-shifted replica of the input pulse, in accordance

with the Fourier shift-theorem. A $\lambda/2$-plate in front of the shaper served to rotate the input pulse polarization and thereby control the relative intensity of the two output pulses. As was demonstrated in [8] in an all-optical experiment, the temporal separation τ between both pulses can be controlled with a precision down to 300 zs. In the quantum control experiments described in the following we varied τ around a base value of $\tau_0 = 120$ fs in order to separate both pulses in time and prevent optical interferences. By this means we made sure that the exerted control relies solely on the coherent manipulation of quantum interferences.

Experimental results for a delay variation spanning more than one optical period of 2.65 fs with a step resolution of 41.5 as are presented in Fig. 1.15(a) and (b). The photoelectron spectra shown in (a) exhibit clear signatures of ultrafast switching between the AT channels S and F due to PL, as discussed in Sec. 1.3.2.2. The electronic response to the subtle changes in the optical phase becomes most transparent in the AT contrast

$$C = \frac{F - S}{F + S} \tag{1.41}$$

derived from the photoelectron spectra and displayed as a black line in (b). The contrast curve oscillates with a period of one optical cycle as the driven atom switches back and forth between the dressed states. In comparison, the laser power (grey line) which was monitored during the experiments remains constant up to fluctuations of about 1%. Hence the observed contrast oscillation is not correlated with laser intensity variations.

The grey-shaded area in (b) (vertical dashed lines in (a)) highlights one half-cyle of electronic switching. The strictly monotonic behavior of the AT contrast in this interval demonstrates the controllability of the underlying electron dynamics on a temporal level of 41.5 as. In order to explore the limits of this controllability we performed a second scan in this interval with an increased resolution of 8.6 as. The results, which are displayed in Fig. 1.15(c) and (d), reveal only slight deviations from strict monotony. This demonstrates, that the controllability is significantly increased down to the sub-10 as regime. Again, the tendency of the contrast curve to decline with increasing pulse separation is a pure phase effect, since the laser power remained constant up to 1% fluctuations.

1.6 Ultrafast Efficient Switching of Concerted Electron-Nuclear Dynamics in Molecules

One of the longterm goals of coherent control is the steering of photochemical processes in large bio-molecules [115]. As a first step towards systems of higher complexity we extend the principles of SPODS as discussed in the previous sections from atomic model systems to the strong-field control of coherent electron dynamics in a prototype molecule. As a reminder, the basic physical

mechanism behind SPODS realized by shaped femtosecond laser pulses can be summarized as follows: The initial part of the shaped pulse resonantly excites a coherent charge oscillation of maximum amplitude. By tailoring the optical phase of the driving laser field to the phase of the induced dipole oscillation the energy of the interacting system is either increased (upper dressed state) or decreased (lower dressed state). As a result higher or lower energy target channels open up and can be addressed selectively. In general, the situation in molecules is much more complicated than in atoms. Along with the electronic excitation vibrational dynamics are launched, that will affect both the amplitude and the phase of the induced charge oscillation due to the coupling between electronic and nuclear degrees of freedom. A maximum amplitude of the electric dipole oscillation, as required for full selectivity, is obtained only for a maximum overlap of the nuclear wave packets in the ground and excited state. The propagation of nuclear wave packets during the preparation of coherence thus hampers the build-up of the dipole oscillation. Moreover, the wave packet propagation leads to a continuous variation of the electronic resonance, i.e. Bohr frequency. This changes the eigenfrequency of the electric dipole and results in an additional phase drift which the laser field has to adapt to in order to maintain a defined phase relation to the dipole. Therefore, simple pulse shapes such as double-pulse sequences or linearly chirped pulses are not expected to be optimal for the efficient control of coupled electron-nuclear dynamics in molecules.

For our studies we chose the potassium dimer (K_2) as a molecular prototype system, since K_2 can be treated experimentally [73, 74] and theoretically [83, 116, 117] on a highly accurate level. The relevant potential energy surfaces (PES) of K_2 are shown in Figure 1.16(a). Before the interaction with the laser the molecule resides in the ground-state $X^1\Sigma_g^+$. Upon irradiation with a weak 790 nm, 25 fs FWHM laser pulse the $2^1\Pi_g$ state is excited by a resonant two-photon absorption process via the intermediate state $A^1\Sigma_u^+$. Higher lying electronic states such as $5^1\Sigma_g^+$, $6^1\Sigma_g^+$ and $3^1\Pi_g$ are energetically inaccessible under perturbative interaction. In the experiment the molecule is post-ionized by a second, delayed probe pulse with a central wavelength of 570 nm. The probe pulse maps the final population of the target states $2^1\Pi_g$ and $5^1\Sigma_g^+$ into the photoelectron spectrum. Its central wavelength was chosen to ensure background-free detection of the relevant two-color photoelectron signals as seen in the inset to Fig. 1.16(b). The corresponding photoelectron spectrum for excitation with a weak IR pulse is shown at the front of Figure 1.16(b). It shows a weak contribution from the $2^1\Pi_g$ state around $E_{kin} = 1.0$ eV and almost no electrons from the $5^1\Sigma_g^+$ state around $E_{kin} = 1.25$ eV. All spectra in Figure 1.16 (b) are recorded using a BWL IR pulse. When interacting with an intense resonant laser pulse however an electronic coherence between the $X^1\Sigma_g^+$ state and the $A^1\Sigma_u^+$ state is created, i.e. a charge oscillation is launched by the laser field. In analogy to the dressed states in atoms the Light-Induced Potentials (LIPs; indicated by the line segments above and below the $A^1\Sigma_u^+$ state) split up due to the strong coupling between the bare states $X^1\Sigma_g^+$ and

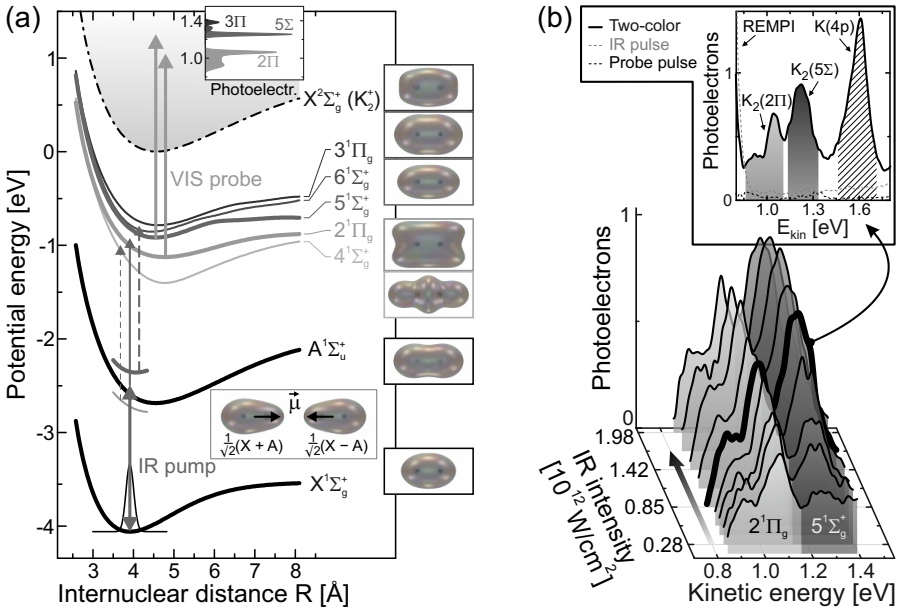

Figure 1.16 (a) Potential energy surfaces of K_2. (b) Photoelectron spectra for different intensities of the BWL IR pump pulse ranging from the weak-field regime (front), where only the target state $2^1\Pi_g$ state is excited, into the non-perturbative strong-field regime (back), where new target states such as the $5^1\Sigma_g^+$ state become energetically accessible as well and are populated efficiently. Inset to (b): One- and two-color photoelectron spectra to demonstrate background-free detection of the relevant photoelectron signals from the molecular target states.

$A^1\Sigma_u^+$. If the driving laser field is intense enough, i.e. the splitting induced in the $X^1\Sigma_g^+$-$A^1\Sigma_u^+$ (X-A) subsystem is sufficiently large, the higher-lying states $5^1\Sigma_g^+$, $6^1\Sigma_g^+$ and $3^1\Pi_g$ become energetically accessible as well and can be populated efficiently. Hence the steep rise of the $5^1\Sigma_g^+$-contribution observed in Figure 1.16(b) with increasing IR laser intensity. At an intensity of $I_0 = 8.5 \cdot 10^{11}$ W/cm^2 the $5^1\Sigma_g^+$ signal already dominates the spectrum, indicating more efficient population of the upper target state as compared to the lower target state $2^1\Pi_g$ by the unshaped pulse. The reason for this asymmetry is a slight blue-detuning of the IR laser spectrum with respect to the X-A-resonance, which is 830 nm for the equilibrium internuclear separation of $R_0 = 3.9$ Å. As a consequence the induced dipole tends to oscillate in anti-phase with the driving laser field already upon creation, favoring the upper LIP and biasing the system towards the upper target state $5^1\Sigma_g^+$.

Under the experimental conditions described above the manifold of target states is sub-divided into two sets of states which we refer to as the lower target channel, comprising states $4^1\Sigma_g^+$ and $2^1\Pi_g$, and the upper target channel,

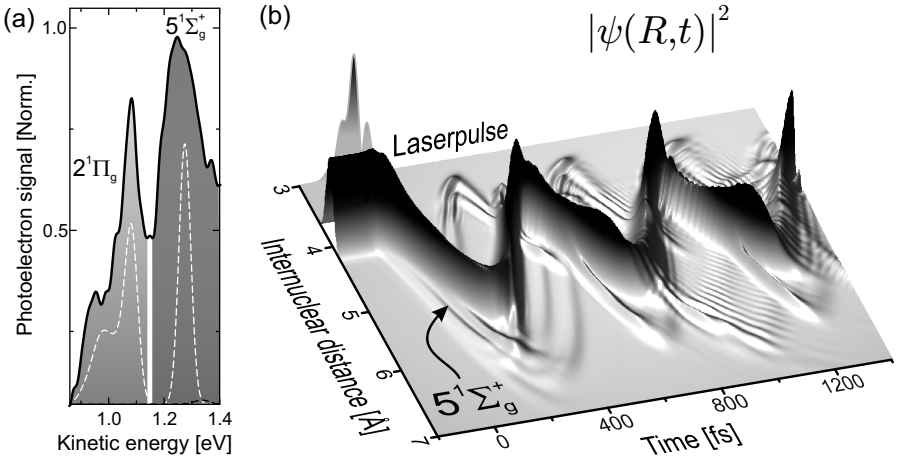

Figure 1.17 (a) Measured photoelectron spectrum together with calculated photoelectron signals (dashed white lines). (b) Calculated wavepacket dynamics in the $5^1\Sigma_g^+$ state after excitation with the shaped femtosecond laser pulse.

comprising states $5^1\Sigma_g^+$, $6^1\Sigma_g^+$ and $3^1\Pi_g$. The target states $2^1\Pi_g$ and $5^1\Sigma_g^+$, however, are the most relevant representatives of each target channel. Therefore we will continue to consider only the lower target state $2^1\Pi_g$ and and the upper target state $5^1\Sigma_g^+$ in the following discussion. The control objective is then to design shaped laser pulses which selectively populate only one of these target states. In the control experiments we pursued an a physically motivated approach based on multi-pulse sequences from sinusoidal spectral phase-modulation (cf. Sec. 1.3.3.1). As discussed in Sec. 1.2.1 this class of spectral phase-modulations provides a great variety of tailored laser fields ranging from regularly shaped multi-pulse sequences to complex shaped single pulses. Due to this versatility, sinusoidally phase-modulated laser pulses are well-suited to adapt to the richness of dynamics and processes encountered in complex molecular systems. A coarse-grain scan of the parameter space $\{A;T;\phi\}$ revealed a high degree of control over the population on both the upper and the lower target state for a sine-amplitude of $A = 0.8$. For this amplitude a maximum of the signal from the upper target state was found at $T = 50$ fs and $\phi = 1.8$ rad. The two-color photoelectron spectrum, recorded after the excitation with the shaped control pulse, is shown in Figure 1.17(a). The signal assigned to the $5^1\Sigma_g^+$ clearly exceeds the signal from the $2^1\Pi_g$ state. In the spirit of the control experiments on atoms discussed in Sec. 1.3.2.2, we varied the sine-phase ϕ by half an optical cycle, i.e. $\Delta\phi = \pi$, in order to invert the picture. The resulting photoelectron spectrum is shown in Figure 1.18(a). Indeed, the spectrum is dominated by the $2^1\Pi_g$-photoelectrons indicating efficient and selective switching from the upper to the lower target state by turning just a single parameter on the control field. The ensuing

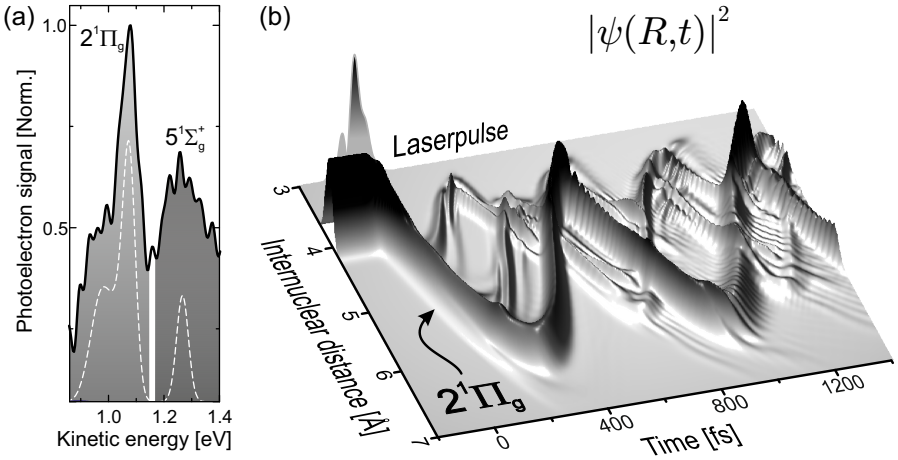

Figure 1.18 (a) Measured photoelectron spectrum together with calculated photoelectron signals (dashed white lines). (b) Calculated wavepacket dynamics in the $2^1\Pi_g$ state after excitation with the shaped femtosecond laser pulse.

nuclear dynamics in the states $5^1\Sigma_g^+$ and $2^1\Pi_g$, extracted from the simulated population dynamics discussed in the following, are shown in Fig. 1.17(b) and 1.18(b), respectively. These plots vizualize the distinct nuclear wavepacket dynamics launched in the molecule by the selective excitation of a specific electronic target state. The different roundtrip-times for the wavepacket can clearly be seen along with the different ranges of internuclear separations that are covered.

To illuminate the physical mechanism behind the efficient population of a preselected molecular target state we employ quantum dynamics simulations and analyze the interaction of K_2 molecules with shaped femtosecond laser pulses [74]. The calculated neutral population dynamics induced by the shaped laser field for the selective population of the upper target state are shown in Fig. 1.19(a). Initially, around $t = -50$ fs, the rising edge of the shaped laser pulse excites the molecule and induces an electronic coherence in the resonant X-A-subsystem, i.e. prepares a coherent charge oscillation (cf. frame (iv)). The central wavelength of the laser pulse is blue detuned with respect to the $X^1\Sigma_g^+$-$A^1\Sigma_u^+$ resonance. As a consequence the induced dipole follows the driving laser field with a phase shift of π, as observed in the dipole and field oscillations shown in frame (ii). However, during the ensuing interaction with the laser pulse the electronic coherence is influenced by vibrational wavepacket dynamics. The internuclear distance increases due to the wavepacket propagation on the excited state PES, and the resonance frequency of the X-A-subsystem decreases in accordance with the decreasing difference potential. This change in the eigenfrequency of the dipole alters the phase relation between dipole and field, and the out-of-phase oscillation re-

quired for the maximization of the interaction energy is perturbed. Due to the temporally varying phase $\zeta(t)$, i.e. detuning $\Delta(t)$, of the tailored laser pulse (black line in frame (*iii*)), however, the field is able to adapt to the changes in the dipole phase and maintain the desired phase relation. Around $t = 0$ fs the most intense part of the laser pulse opens the upper target channel energetically. In this time window the LIP splitting induced in the X-A-subsystem, indicated by the dashed lines in frame (*i*), is sufficient to shift the upper LIP into resonance with the energy of the $5^1\Sigma_g^+$ state (bold black line), as marked by the grey circle. By virtue of the maximized interaction energy the population is steered efficiently into the upper target state which is populated by 75% by the end of the pulse. Although the lower target state (thin grey line in frame (*i*)) is energetically accessible throughout the entire interaction, the phase relation between electric field and induced charge oscillation prevents any efficient population transfer. A detailed analysis of the vibrational wavepacket dynamics reveals that the internuclear distance increases by 9% between the build-up of the coherence at $t = -50$ fs and the population transfer to the upper target state, implying a change of the X-A Bohr-frequency of 110 meV.

The simulation results for the selective population of the lower target state $2^1\Pi_g$ are shown in Fig. 1.19(b). Again the X-A-subsystem is initially guided into a state of electronic coherence around $t = -50$ fs. Subsequently, after some Rabi-type oscillations 60% of the population is transferred to the lower target state. The transient population return to the X-A-subsystem observed in this case is mainly due to the strong coupling between states $A^1\Sigma_u^+$ and $2^1\Pi_g$, as compared to the coupling between states $A^1\Sigma_u^+$ and $5^1\Sigma_g^+$ [83]. Moreover the lower target state is always accessible energetically, whereas an efficient population transfer to (or from) the upper target state can only occur in a short time window of maximum field intensity. The induced dipole oscillation analyzed with respect to the laser electric field (see frame (*ii*)) reveals that the final population transfer to the lower target state is indeed based on the in-phase oscillation of dipole and field (right panel in (*ii*)) and the corresponding minimization of the interaction energy. Despite the blue-detuning of the laser central frequency, which initially still promotes the out-of-phase oscillation (left panel in (*ii*)), the tailored electric field adapts to the induced dipole dynamics in the course of the interaction and triggers the efficient population of state $2^1\Pi_g$ around $t = 50$ fs.

Frame (*i*) shows the LIP splitting induced in the X-A-subsystem (dashed lines) along with the energies of the $5^1\Sigma_g^+$ state (thin grey line) and the $2^1\Pi_g$ state (bold black line) at $\langle R \rangle(t)$, i.e. the expectation value of the internuclear separation as a function of time. At early times, around $t = -50$ fs when dipole and field still oscillate out-of-phase, the induced LIP splitting is not yet large enough to enable an efficient population transfer to the upper target state. During the most intense part of the pulse around $t = 0$ fs, on the other hand, the upper target state would be accessible energetically. In this time window however, dipole and field already oscillate in-phase (not shown) so

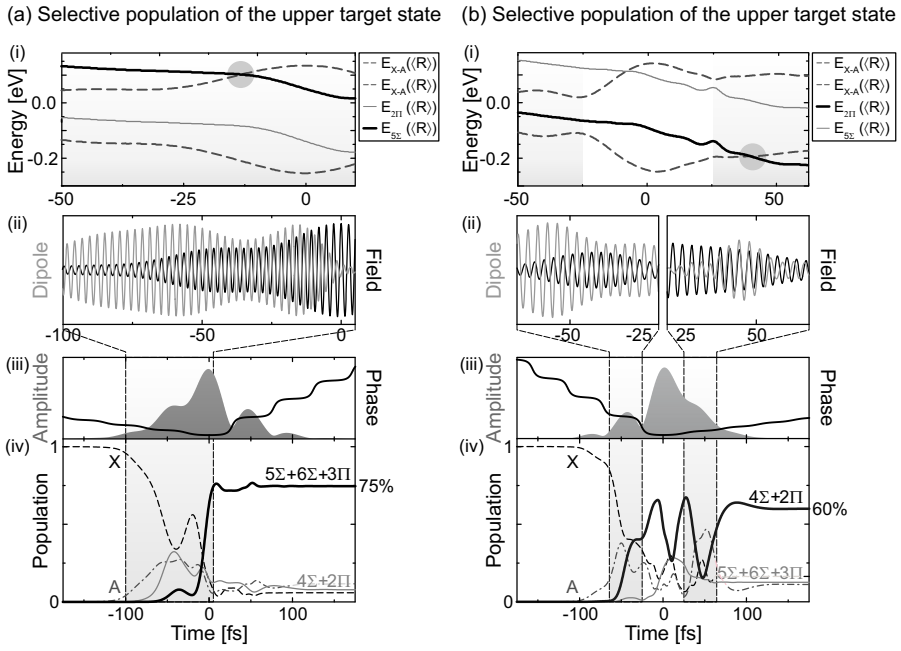

Figure 1.19 Quantum dynamics simulations for the two distinct situations of selective population of the (a) upper and (b) the lower target state. The frame (iv) shows the population dynamics induced by the shaped laser field pictured in (iii). The remaining panels depict (ii) the oscillations of the laser field together with the induced dipole-moment and (i) the induced energetic splitting in the X-A-subsystem along with the accessibility of the target states. Grey backgrounds highlight the relevant time windows that are discussed in the text.

that here also no population is transferred to the upper target state. Instead at slightly later times around $t = 50$ fs the energy of the $2^1\Pi_g$ state shifts into resonance with the lower LIP of the X-A-subsystem, as marked by the grey circle. Because this LIP is populated due to the in-phase oscillation of field and dipole (cf. grey-shaded time window in frame (ii)) the population is transferred efficiently to the lower target state. The interaction time of the molecule with the laser pulse between the build-up of the electronic coherence, i.e. the coherent charge oscillation, around $t = -50$ fs and the final population transfer at $t = +50$ fs is longer than in the case of the upper target state. The nuclear dynamics during this time period entail a larger variation of the internuclear separation and, moreover, are more complex than in the first case. The X-A Bohr-frequency decreases by 190 meV which corresponds to 130 nm as the internuclear distance changes by 18%.

For transparency in the preceding discussion we assumed the shaped IR pulses to be polarized at 45° with respect to the internuclear axis of the diatomic molecule. Thus, parallel ($\Sigma \leftarrow \Sigma$) and perpendicular ($\Pi \leftarrow \Sigma$) transitions to

the various electronic target states are driven by the same intensity. For the actual comparison between measured and simulated photoelectrons, as seen in Figs. 1.17 and 1.18 we considered both focal intensity averaging and molecular orientation averaging, in order to model the experimental conditions. Details about the averaging procedures performed can be found in [74]. The agreement between the measured and the simulated photoelectron signals justifies our interpretations based on the calculated quantum dynamics.

In conclusion, the concept of SPODS as discussed on atomic systems in the preceding sections is readily extended to the control of coupled electron-nuclear dynamics in molecules. The concept of tailoring the intricate interplay between the induced charge oscillation and the driving laser field by adapting the optical phase to the induced dipole dynamics and introducing directed Stark shifts via the field amplitude, is also applicable to the efficient and selective excitation of bound target states in molecules – that may even be completely inaccessible in the case of perturbative (weak-field) interactions. The additional phase dynamics in molecules due to the coupling of electronic and nuclear degrees of freedom may result in a less straight-forward implementation (and interpretation) of the control scheme. However, tailored femtosecond laser pulses that offer a wide range of pulse shapes, temporally structured in terms of amplitude, phase and polarization profile, and benefit from strong dipole couplings between the bound states of molecules, are ideally suited to realize control over the concerted electron-nuclear dynamics.

For applications to chemistry, a validation of coherent control strategies on even larger molecules is important. As a first step, we investigated the mass spectra from the dissociation of isopropyl alcohol using a photon locking sequence. The molecular ion yield shows pronounced variations upon changes of the temporal phase in the pulse sequence [28, 118]. In these experiments the ion yield from potassium atoms was measured simultaneously and showed no significant variations. This result confirms that no spectral/spatial cross-sensitivities are introduced by our pulse shaper. The observations show that the optical phase of the shaped pulse exerts control over the molecular dynamics of isopropyl alcohol. The phase dependence of the signal is hinting to a SPODS mechanism, however, systematic studies on the intensity dependence for a final proof have not been performed so far. Further indications that SPODS in general and photon locking as a specific example are important strong-field mechanisms come from theoretical considerations. SPODS shows up as an optimal solution in optimal control theory of the potassium dimer [116]. Furthermore in [93] it was found that photon locking is a key ingredient for the excitation of ground-surface vibrational motion while minimizing radiation damage.

1.7 Conclusions

We have demonstrated a strong-field control scenario based on the Selective Population of Dressed States (SPODS). We derived the theoretical background in terms of both classical physics and quantum mechanics. We showed tunability of this bidirectional Stark effect up to nearly 300 meV, a selectivity of almost up to 100% and a precision down to the sub-10 attosecond regime experimentally on atoms and molecules with a theoretical efficiency up to 100%.

Note that SPODS is nearly always operative in resonant strong-field excitation using modulated ultrashort laser pulses, the only exception being so-called real laser pulses [77, 72] (i.e. electric fields with only one quadrature in the complex plane) that are usually hard to achieve in ultrafast laser technology. This is why many different pulse shapes can lead to comparable dressed state energy shifts and dressed state populations. We suggested that SPODS is operative in larger systems as well. This could explain why optimized pulses from adaptive feedback control experiments often do not exhibit a unique structure: (*i*) due to the multi-photon nature of the excitation, relatively strong fields are often at play automatically and (*ii*) the higher the total excitation the higher the density of excited states. It is therefore very likely to establish the non-perturbative resonant excitation conditions where SPODS can be operative to switch population to different target states.

Now that this mechanism is understood, relatively simple ultrashort optimal pulse shapes can be used for implementation of this robust approach for laser control of photophysical systems.

Looking ahead, coherent laser pulses covering the complete spectral range of valence bond excitation from the UV to the IR spectral region are becoming available (see for example [119]), and we expect SPODS to increase in importance in coherently controlled photochemistry with applications ranging from reaction control within molecules up to discrimination between different molecules in a mixture and laser based quantum information technologies.

1.8 Acknowledgements

We are grateful for Moshe Shapiro's constant supportive and enlightening input to discussions (both to scientific topics and to life and culture in general) especially during several visits to our laboratories within the framework of a "Research Award of the Alexander von Humboldt Foundation" from 2009 to 2012.

Furthermore, financial support by the Deutsche Forschungsgemeinschaft (DFG) via the project WO-848/3 is acknowledged.

REFERENCES

[1] M. Shapiro and P. Brumer. *Quantum control of molecular processes.* Wiley, Berlin, (2011).

[2] A.M. Weiner. *Opt. Comm.*, **284**:3669–3692, (2011).

[3] D. Goswami. *Phys. Rep.*, **374**:385–481, (2003).

[4] M. Wollenhaupt, A. Assion, and T. Baumert. *in Springer Handbook of Lasers and Optics, 2nd Edition, Ch. 12: Short and Ultrashort Laser Pulses.* Springer, New York, (2012).

[5] D. B. Strasfeld, S.-H. Shim, and M. T. Zanni. *New Advances in Mid-IR Pulse Shaping and its Application to 2D IR Spectroscopy and Ground-State Coherent Control*, pages 1–28. Wiley, (2009).

[6] A. Monmayrant, S. Weber, and B. Chatel. *J. Phys. B*, **43**:103001, (2010).

[7] T. Brixner and G. Gerber. *Opt. Lett.*, **26**:557–559, (2001).

[8] J. Köhler, M. Wollenhaupt, T. Bayer, C. Sarpe, and T. Baumert. *Opt. Expr.*, **19**:11638–11653, (2011).

[9] A.H. Zewail. *J. Phys. Chem. A*, **104**:5660–5694, (2000).

[10] J. Manz and L. Woeste. *Femtosecond Chemistry.* Wiley-VCH, Weinheim, (1995).

[11] S.A. Rice and M. Zhao. *Optical control of molecular dynamics.* Wiley, New York, (2000).

Please enter `\offprintinfo{(Title, Edition)}{(Author)}`
`at the beginning of your document.`

[12] D. Tannor. *Introduction to Quantum Mechanics: A Time-Dependent Perspective*. Palgrave MacMillan, Hampshire, (2007).

[13] D.J. Tannor and S.A. Rice. *Advances in Chemical Physics: Evolution of Size Effects in Chemical Dynamics Part 1*, **70**:441–523, (1988).

[14] M. Shapiro and P. Brumer. *Int. Rev. Phys. Chem.*, **13**:187–229, (1994).

[15] T. Baumert, J. Helbing, and G. Gerber. In *Advances in Chemical Physics: Chemical Reactions and their Control on the Femtosecond Time Scale: 20th Solvay Conference on Chemistry*, volume **101**, pages 47–82. Wiley Online Library, (1997).

[16] H. Rabitz, R. de Vivie-Riedle, M. Motzkus, and K. Kompa. *Science*, **288**:824–828, (2000).

[17] M. Shapiro and P. Brumer. *Rep. Prog. Phys.*, **66**:859, (2003).

[18] M. Dantus and V.V. Lozovoy. *Chem. Rev.*, **104**:1813–1860, (2004).

[19] V. Bonacic-Koutecký and R. Mitric. *Chem. Rev.*, **105**:11–66, (2005).

[20] T. Brixner, T. Pfeifer, G. Gerber, M. Wollenhaupt, and T. Baumert. Optimal control of atomic, molecular and electron dynamics with tailored femtosecond laser pulses. In *Femtosecond Laser Spectroscopy*, pages 225–266. Springer, (2005).

[21] M. Wollenhaupt, V. Engel, and T. Baumert. *Annu. Rev. Phys. Chem.*, **56**:25–56, (2005).

[22] P. Nuernberger, G. Vogt, T. Brixner, and G. Gerber. *Phys. Chem. Chem. Phys.*, **9**:2470–2497, (2007).

[23] J. Werschnik and E. K. U. Gross. *J. Phys B*, **40**:R175, (2007).

[24] W. Wohlleben, T. Buckup, J.L. Herek, and M. Motzkus. *Chem. Phys. Chem.*, **6**:850–857, (2005).

[25] Y. Silberberg. *Chem. Phys. Chem.*, **60**:277–292, (2009).

[26] K. Ohmori. *Ann. Rev. Phys. Chem.*, **60**:487–511, (2009).

[27] C. Brif, R. Chakrabarti, and H. Rabitz. *New J. Phys.*, **12**:075008, (2010).

[28] M. Wollenhaupt and T. Baumert. *Faraday Discuss.*, **153**:9–26, (2011).

[29] P. Gaspard and I. Burghardt (eds.). *Advances in Chemical Physics: Chemical Reactions and Their Control on the Femtosecond Time Scale, XXth Solvay Conference on Chemistry*. Wiley, New York, (1997).

[30] J.L. Herek. *J. Photochem. Photobiol. A*, **180**:225, (2006).

[31] H. Fielding, M. Shapiro, and T. Baumert. *J. Phys. B*, **41**:070201, (2008).

[32] H. Rabitz. *New. J. Phys.*, **11**:105030, (2009).

[33] H. Fielding and A. Robb. *Phys. Chem. Chem. Phys.*, **12**:15569, (2010).

[34] R.S. Judson and H. Rabitz. *Phys. Rev. Lett.*, **68**:1500–1503, (1992).

[35] T. Baumert, T. Brixner, V. Seyfried, M. Strehle, and G. Gerber. *Appl. Phys. B*, **65**:779–782, (1997).

[36] D. Meshulach, D. Yelin, and Y. Silberberg. *Opt. Comm.*, **138**:345–348, (1997).

[37] C. J. Bardeen, V. V. Yakovlev, K. R. Wilson, S. D. Carpenter, P. M. Weber, and W. W. S. Warren. *Chem. Phys. Lett.*, **280**:151–158, (1997).

[38] A. Assion, T. Baumert, M. Bergt, T. Brixner, B. Kiefer, V. Seyfried, M. Strehle, and T. Gerber. *Science*, **282**:919–922, (1998).

[39] R. J. Levis and H. A. Rabitz. *J. Phys. Chem. A*, **106**:6427–6444, (2002).

[40] C. Daniel, J. Full, L. González, C. Lupulescu, J. Manz, A. Merli, Š Vajda, and L. Wöste. *Science*, **299**:536–539, (2003).

[41] T. Hornung, R. Meier, and M. Motzkus. *Chem. Phys. Lett.*, **326**:445–453, (2000).

[42] A. Bartelt, A. Lindinger, C. Lupulescu, Š. Vajda, and L. Wöste. *Phys. Chem. Chem. Phys.*, **5**:3610–3615, (2003).

[43] S. Fechner, F. Dimler, T. Brixner, G. Gerber, and D.J. Tannor. *Opt. Expr.*, **15**:15387–15401, (2007).

[44] T. Bayer, M. Wollenhaupt, and T. Baumert. *J. Phys. B*, **41**:074007, (2008).

[45] S. Ruetzel, C. Stolzenberger, F. Dimler, D.J. Tannor, and T. Brixner. *Phys. Chem. Chem. Phys.*, **13**:8627–8636, (2011).

[46] M. Wollenhaupt, A. Präkelt, C. Sarpe-Tudoran, D. Liese, and T. Baumert. *J. Mod. Opt.*, **52**:2187–2195, (2005).

[47] H. A. Rabitz, M. M. Hsieh, and C. M. Rosenthal. *Science*, **303**:1998–2001, (2004).

[48] N.V. Vitanov, T. Halfmann, B.W. Shore, and K. Bergmann. *Annu. Rev. Phys. Chem.*, **52**:763–809, (2001).

[49] B. W. Shore. *Acta Phys. Slov.*, **58**:243–486, (2008).

[50] J.S. Melinger, S.R. Gandhi, A. Hariharan, J.X. Tull, and W.S. Warren. *Phys. Rev. Lett.*, **68**:2000, (1992).

[51] I.R. Solá, J. Santamaría, and V.S. Malinovsky. *Phys Rev. A*, **61**:043413, (2000).

[52] V.S. Malinovsky and J.L. Krause. *Eur. Phys. J. D*, **14**:147–155, (2001).

[53] M. Krug, T. Bayer, M. Wollenhaupt, C. Sarpe-Tudoran, S.S. Ivanov T. Baumert, and N.V. Vitanov. *New J. Phys.*, **11**:105051, (2009).

[54] S. Zhdanovich, E. A. Shapiro, M. Shapiro, J. W. Hepburn, and V. Milner. *Phys. Rev. Lett.*, **100**:103004, (2008).

[55] C. Trallero-Herrero, J.L. Cohen, and T. Weinacht. *Phys. Rev. Lett.*, **96**:063603, (2006).

[56] T. Frohnmeyer, M. Hofmann, M. Strehle, and T. Baumert. *Chem. Phys. Lett.*, **312**:447–454, (1999).

[57] B.J. Sussman, D. Townsend, M.Y. Ivanov, and A. Stolow. *Science*, **314**:278–281, (2006).

[58] T. Baumert, V. Engel, Ch. Meier, and G. Gerber. *Chem. Phys. Lett.*, **200**:488–494, (1992).

[59] H. Goto, H. Katsuki, H. Ibrahim, H. Chiba, and K. Ohmori. *Nature Phys.*, **7**:383–385, (2011).

[60] B.J. Sussman. *Am. J. Phys.*, **79**:477–484, (2011).

[61] P.B. Corkum and F. Krausz. *Nature Phys.*, **3**:381–387, (2007).

[62] M.F. Kling and M.J.J. Vrakking. *Annu. Rev. Phys. Chem.*, **59**:463–492, (2008).

[63] F. Krausz and M. Ivanov. *Rev. Mod. Phys.*, **81**:163–234, (2009).

[64] F. Remacle and R.D. Levine. *Proc. Nat. Aca. Sci.*, **103**:6793–6798, (2006).

[65] S.H. Autler and C. H. Townes. *Phys. Rev.*, **100**:703, (1955).

[66] Ch. Meier and V. Engel. *Phys. Rev. Lett.*, **73**:3207, (1994).

[67] M. Wollenhaupt, A. Assion A, O. Bazhan, C. Horn, D. Liese, C. Sarpe-Tudoran, M. Winter, and T. Baumert. *Phys. Rev. A*, **68**:015401, (2003).

[68] M. Wollenhaupt, D. Liese, A. Präkelt, C. Sarpe-Tudoran, and T. Baumert. *Chem. Phys. Lett.*, **419**:184–190, (2006).

[69] A. Palacios, H. Bachau, and F. Martín. *Phys. Rev. A*, **75**:013408, (2007).

[70] T. Bayer, M. Wollenhaupt, C. Sarpe-Tudoran, and T. Baumert. *Phys. Rev. Lett.*, **102**:023004, (2009).

[71] M. Wollenhaupt, T. Bayer, N.V. Vitanov, and T. Baumert. *Phys. Rev. A*, **81**:053422, (2010).

[72] M. Wollenhaupt, A. Präkelt, C. Sarpe-Tudoran, D. Liese, and T. Baumert. *Appl. Phys. B*, **82**:183–188, (2006).

[73] T. Bayer, H. Braun, C. Sarpe, R. Siemering, P. von den Hoff, R. de Vivie-Riedle, T. Baumert, and M. Wollenhaupt. *Phys. Rev. Lett.*, **110**:123003, (2013).

[74] H. Braun, T. Bayer, C. Sarpe, R. Siemering, R. de Vivie-Riedle, T. Baumert, and M. Wollenhaupt. *J. Phys. B*, **47**:124015, (2014).

[75] D. Meshulach and Y. Silberberg. *Nature*, **396**:239–242, (1998).

[76] A. Präkelt, M. Wollenhaupt, C. Sarpe-Tudoran, and T. Baumert. *Phys. Rev. A*, **70**:063407, (2004).

[77] N. Dudovich, T. Polack, A. Pe'er, and Y. Silberberg. *Phys. Rev. Lett.*, **94**:083002, (2005).

[78] M. Wollenhaupt, A. Präkelt, C. Sarpe-Tudoran, D. Liese, and T. Baumert. *J. Opt. B*, **7**:270–276, (2005).

[79] M. Wollenhaupt, A. Präkelt, C. Sarpe-Tudoran, D. Liese, T. Bayer, and T. Baumert. *Phys. Rev. A*, **73**:063409, (2006).

[80] J.L. Herek, W. Wohlleben, R.J. Cogdell, D. Zeidler, and M. Motzkus. *Nature*, **417**:533–535, (2002).

[81] V.V. Lozovoy, I. Pastirk, A. Walowicz, and M. Dantus. *J. Chem. Phys.*, **118**:3187–3196, (2003).

[82] N. Dudovich, D. Oron, and Y. Silberberg. *J. Chem. Phys.*, **118**:9208, (2003).

[83] M. Wollenhaupt and T. Baumert. *J. Photochem. Photobiol. A*, **180**:248–255, (2006).

[84] J. Hauer, T. Buckup, and M. Motzkus. *J. Chem. Phys.*, **125**:061101, (2006).

[85] J. Voll and R. Vivie-Riedle. *New J. Phys.*, **11**:105036, (2009).

[86] B. Broers, H.B. van Linden van den Heuvell, and L.D. Noordam. *Phys. Rev. Lett.*, **69**:2062–2065, (1992).

[87] C.J. Bardeen, Q. Wang, and C.V. Shank. *Phys. Rev. Lett.*, **75**:3410–3413, (1995).

[88] A. Assion, T. Baumert, J. Helbing, V. Seyfried, and G. Gerber. *Chem. Phys. Lett.*, **259**:488–494, (1996).

[89] J. Degert, W. Wohlleben, B. Chatel, M. Motzkus, and B. Girard. *Phys. Rev. Lett.*, **89**:203003, (2002).

[90] R.W. Boyd. *Nonlinear Optics*. Academic Press, New York, (2008).

[91] J.D. Jackson. *Classical Electrodynamics*. Wiley, New York, (1998).

[92] B.W. Shore. *Manipulating Quantum Structures Using Laser Pulses*. Cambridge Univ. Press, Cambridge, (2011).

[93] R. Kosloff, A.D. Hammerich, and D. Tannor. *Phys. Rev. Lett.*, **69**:2172–2175, (1992).

[94] E.T. Sleva, I.M. Xavier Jr, and A. H. Zewail. *J. Opt. Soc. Am. B*, **3**:483–487, (1985).

[95] Y.S. Bai, A.G. Yodh, and T.W. Mossberg. *Phys. Rev. Lett.*, **55**:1277–1280, (1985).

[96] S.R. Hartmann and E.L. Hahn. *Phys. Rev.*, **128**:2042–2053, (1962).

[97] A. Abragam. *The Principles of Nuclear Magnetism*. Clarendon Press (Reprint), Oxford, (1994).

[98] A.A. Rangelov, N.V. Vitanov, L.P. Yatsenko, B.W. Shore, T. Halfmann, and K. Bergmann. *Phys. Rev. A*, **72**:053403, (2005).

[99] J. Cao, C.J. Bardeen, and K.R. Wilson. *Phys. Rev. Lett*, **80**:1406–1409, (1998).

[100] V.S. Malinovsky and J.L. Krause. *Phys. Rev. A*, **63**:043415, (2001).

[101] J. Schneider, M. Wollenhaupt, A. Winzenburg, T. Bayer, J. Köhler, R. Faust, and T. Baumert. *Phys. Chem. Chem. Phys.*, **13**:8733–8746, (2011).

[102] J. Ahn, T. Weinacht, and P.H. Bucksbaum. *Science*, **287**:463–465, (2000).

[103] R. de Vivie-Riedle and U. Troppmann. *Chemical reviews*, **10**:5082–5100, 2007.

[104] C. Zener. *Proc. R. Soc. Lond. A*, **137**:696–702, (1932).

[105] L.D. Landau. *Phys. Z. Sow.*, **2**:46–51, (1932).

[106] J.S. Melinger, Suketu R. Gandhi, A. Hariharan, J.X. Tull, and W.S. Warren. *Phys. Rev. Lett.*, **68**:2000–2003, (1992).

[107] R. Netz, T. Feurer, G. Roberts, and R. Sauerbrey. *Phys. Rev. A*, **65**:043406, (2002).

[108] B. Chatel, J. Degert, S. Stock, and B. Girard. *Phys. Rev. A*, **68**:041402, (2003).

[109] A. Präkelt, M. Wollenhaupt, A. Assion, C. Horn, C. Sarpe-Tudoran, M. Winter, and T. Baumert. *Rev. Sci. Instr.*, **74**:4950–4953, (2003).

[110] M. Wollenhaupt, M. Krug, J. Köhler, T. Bayer, C. Sarpe-Tudoran, and T. Baumert. *Appl. Phys. B*, **95**:245–259, (2009).

[111] A. Scrinzi, M.Y. Ivanov, R. Kienberger, and D. Villeneuve. *J. Phys. B*, **39**:R1–R37, (2006).

[112] P.H. Bucksbaum. *Science*, **317**:766–769, (2007).

[113] B. von Vacano, T. Buckup, and M. Motzkus. *Opt. Lett.*, **31**:1154–1156, (2006).

[114] A. Galler and T. Feurer. *Appl. Phys. B*, **90**:427–430, (2008).

[115] V.I. Prokhorenko, A.M. Nagy, S.A. Waschuk, L.S. Brown, R.R. Birge, and J.D. Miller. *Science*, **313**:1257–1261, (2006).

[116] P. von den Hoff, M. Kowalewski, and R. de Vivie-Riedle. *Faraday Discuss.*, **153**:159–171, (2011).

[117] J. Petersen, M. Wohlgemuth, B. Sellner, V. Bonacic-Koutecky, H. Lischka, and R. Mitric. *Phys. Chem. Chem. Phys.*, **14**:8299–8306, (2012).

[118] M. Wollenhaupt, T. Bayer, A. Klumpp, C. Sarpe-Tudoran, and T. Baumert. *in Physics and Engineering of New Materials Series: Springer Proceedings in Physics 127*, pages 327–335. Springer, Berlin, (2008).

[119] A. Wirth, M.Th. Hassan, I. Grguraš, J. Gagnon, A. Moulet, T.T. Luu, S. Pabst, R. Santra, Z.A. Alahmed, A.M. Azzeer, V.S. Yakovlev, V. Pervak, F. Krausz, and E. Goulielmakis. *Science*, **334**:195–200, (2011).